Thesis for the Degree of Doctor of Philosophy

A regime shift in the formation of the North Pacific subtropical mode water

북태평양 아열대 모드수 생성 기작의 체제 전환 연구

Sang-Yeob Kim

Advisor: Prof. Ho Jin Lee

August, 2020

Department of Convergence Study on the Ocean Science and Technology

Ocean Science and Technology School
Korea Maritime and Ocean University

본 논문을 김상엽의 이학박사 학위논문으로 인준함

위원장　　이학박사　박 영 규　（인）

위　원　　이학박사　이 호 진　（인）

위　원　　이학박사　김 영 호　（인）

위　원　　이학박사　김 형 석　（인）

위　원　　이학박사　박 균 도　（인）

2020년 7월 22일

한국해양대학교 해양과학기술전문대학원

Table of Contents

List of Tables

List of Figures

A regime shift in the formation of the North Pacific subtropical mode water

Sang-Yeob Kim

Department of Convergence Study on the Ocean Science and Technology
Ocean Science and Technology School
Korea Maritime and Ocean University

Abstract

A regime shift in the formation mechanisms of the North Pacific subtropical mode water (NPSTMW) as well as its causes is investigated using 50-year (1960–2009) ocean general circulation model (OGCM) and 2,000-year pre-industrial simulation of atmosphere-ocean coupled model (Kiel Climate Model). The volume budget analysis suggests that the formation of the NPSTMW is mainly controlled by the air-sea interaction and ocean dynamics. In the OGCM simulation, it is found that there is a regime shift of the relative importance between the two around late-1980s. While the local air-sea interaction process is a main driver of the NPSTMW formation prior to late-1980s, ocean dynamics including the vertical entrainment become dominant since then. The NPSTMW formation is affected by the North Pacific Oscillation simultaneously in the early period, but with a few years lag in the later period. The interdecadal change of the driving mechanism of the interannual variability of the NPSTMW is probably due to stronger (weaker) remote signals in the ocean interior induced by the meridional shift of the Aleutian Low and weaker (stronger) influence of local atmospheric forcing in the western

North Pacific during the former (later) period. Using an atmosphere-ocean coupled model (Kiel Climate Model), it is revealed that the transition of the driving mechanisms for the NPSTMW formation is periodically occurred in multi-decadal timescales. Once the epoch changes, each air-sea interaction and ocean dynamics forcing persists during about 10−30 years. The regime shift of the NPSTMW formation is related to the meridional shift of the Aleutian Low center.

KEY WORDS: North Pacific subtropical mode water, 북태평양 아열대 모드수; ocean general circulation model, 해양 순환 모형; volume budget analysis, 체적 수지 분석; air-sea interaction and upper ocean mixed layer processes, 해양-대기 상호작용 및 해양 상층부 혼합 과정; regime shift, 체제 전환.

Chapter 1. Introduction

The North Pacific subtropical mode water (NPSTMW), which is characterized by a thick subsurface layer of the relatively uniform temperature (16−20°C) and potential density (σ_θ = 24.8−25.7 kg m^{-3}) as well as low potential vorticity (PV < 2.0 × 10^{-10} m^{-1} s^{-1}), is found in the Kuroshio Extension (KE) region (Masuzawa, 1969; Oka & Qiu, 2012) (Figure 1). The NPSTMW affects sea surface temperature (SST), geochemical tracers, and subtropical counter current (Bates, 2012; Kobashi et al., 2006; Oka et al., 2019; Sugimoto & Hanawa, 2007). The NPSTMW subducts into the thermocline with the memory of wintertime SST and reemerges to the surface in the following winter to affect upper-layer distribution of nutrient and the oceanic uptake of the carbon dioxide (Bates, 2012; Oka et al., 2019; Sugimoto & Hanawa, 2007) (Figure 2). In addition, the meridional position of the subtropical counter current is maintained by the horizontal distribution of the NPSTMW (Kobashi et al., 2006), which means that the NPSTMW can affect the oceanic circulation. Therefore, the NPSTMW can be a good indicator for oceanic conditions of the North Pacific.
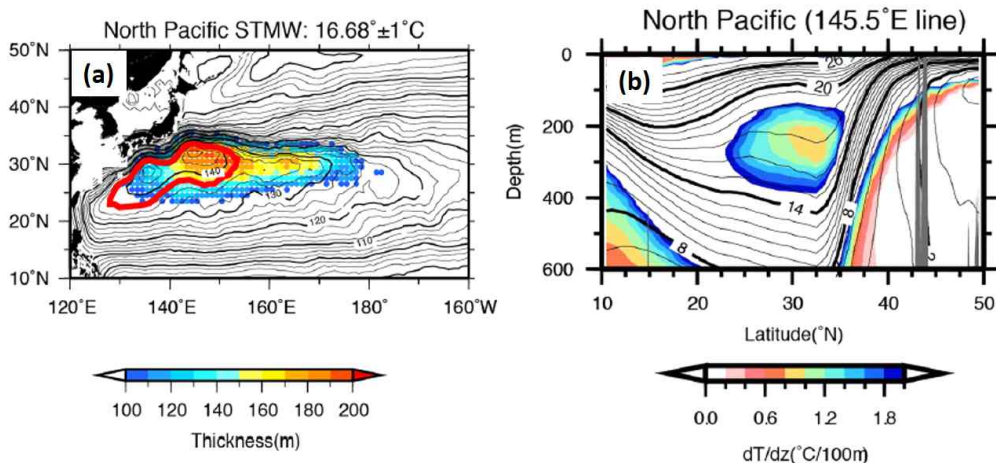
Figure 1. (a) Horizontal distribution of the NPSTMW thickness (m). Thick red contour indicates the recirculation gyre region (Tsubouchi et al., 2016). (b) Meridional section of the vertical temperature gradient (dT/dz, °C per 100 m) along 145.5°E. Black contours represent the isotherms between 0° and 30°C with an interval of 1°C (Tsubouchi et al., 2016).
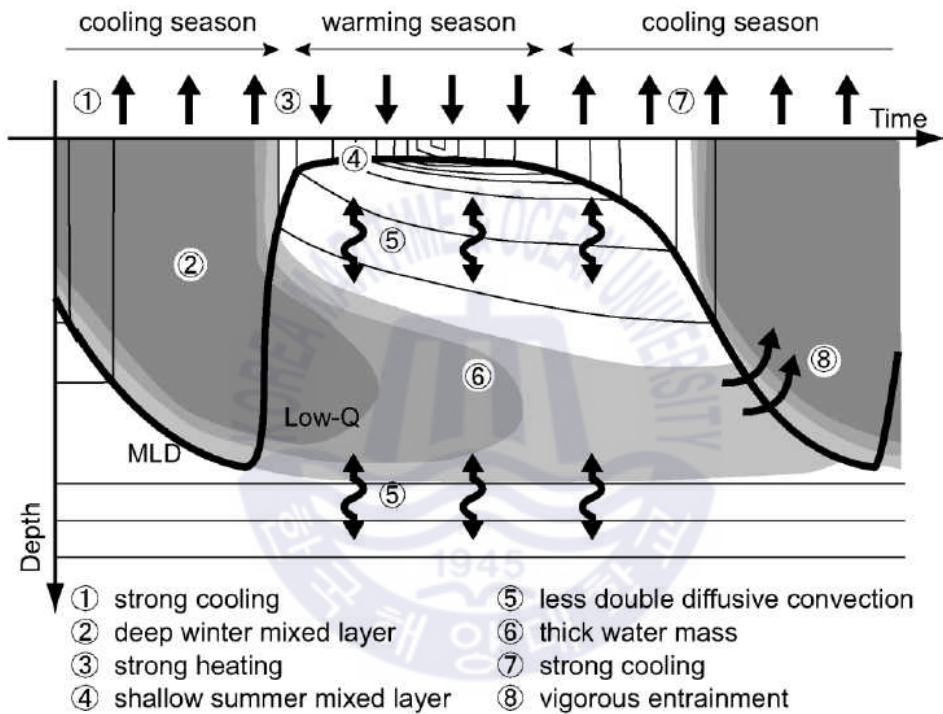
Figure 2. Schematic picture of the NPSTMW re-emergence process (Sugimoto & Hanawa, 2007). Gray shaded indicates the NPSTMW.

Previous studies suggested two different main factors driving the interannual variation of the NPSTMW formation: (1) the ocean mixed layer thermodynamics driven by local air-sea buoyancy flux and (2) the ocean dynamics driven by remote atmospheric wind forcing or local ocean current instability. Hanawa (1987) showed that the NPSTMW is formed at the outcrop area of the SST 16–19°C zone by a

large oceanic heat loss during the cooling season using the hydrographic data from 1970 to 1985. Hanawa and Hoshino (1988) suggested that the air-sea heat transfer is closely related to the formation of the NPSTMW during wintertime from the 10 stations observation data along the section at the south of Japan during 1964−1986. Bingham (1992) also reported that the formation of the NPSTMW has close relationships with the amount of oceanic heat release due to the local atmospheric cooling in winter using the hydrographic data obtained from a few number of stations and the expendable bathythermograph data during 1977−1984.

Meanwhile, Cerovečki and Giglio (2016) suggested that pycnocline depth anomalies have propagated from the central North Pacific and then determine the stratification in the NPSTMW formation area. They showed that the interannual variability of the volume and density of the NPSTMW, using the Argo data during 2005−2012, is affected by the PV anomaly carried by the westward propagating Rossby waves triggered by the basin-scale climate variability. Qiu and Chen (2006) found that the NPSTMW formation is increased (reduced) when the KE is stable (unstable), based on the analysis of the observational data during 1993−2004. However, these studies do not reveal the long-term variability of the NPSTMW formation due to the limitations of the temporal and spatial observational data.

Most of the previous studies on the NPSTMW driving mechanism are largely based on temporally and spatially limited observation, which means the conclusions on the NPSTMW driving mechanism can be different by the different data periods. Because the observed subsurface data is not sufficient to investigate feature of the NPSTMW at long time scales, the long-term ocean model results can be an alternative way to look into the driving mechanism for them. Davis et al. (2011) showed that the seasonal and interannual variability of the NPSTMW volume closely related to the buoyancy loss over the NPSTMW outcropping area at the surface during cooling season from 1979 to 2006 using an eddy-permitting ocean general circulation model (OGCM) with horizontal grid spacing of approximately 18

km. However, it seems that the North Pacific central mode water is merged into the NPSTMW volume in their OGCM, because simulated NPSTMW zonally extends as far east as 170°W, while observed NPSTMW extends as far west as dateline (Tsubouchi et al., 2016). Douglass et al. (2012) suggested with a high-resolution (1/10°) OGCM that the interannual variability of the NPSTMW volume is significantly correlated with a large meander of the Kuroshio path in the south of Japan. However, their model is forced by the climatological mean atmospheric forcing and thereby the interannual variability of the NPSTMW volume in their model only represents the intrinsic ocean variability.

Meanwhile, there are studies reporting the epoch-dependent driving mechanism on the winter upper-layer thermal states in the western North Pacific, based on the basin-scale long-term data or model simulations. According to the previous studies (Pak et al., 2014, 2019; Park et al., 2012), the East-Asia winter monsoon (EAWM) had a greater influence on the winter SST variability in the western North Pacific compared to the influence of the ocean dynamics before around 1990, whereas the opposite is true after around 1990. Sugimoto and Kako (2016) reported that the thermocline change due to the Rossby wave propagation is a main controlling factor for the winter mixed layer depth (MLD) and core-layer temperature of summer NPSTMW in the KE region after late-1980s, while it is the surface heat flux during 1970s–1980s. These researches commonly suggested that a regime shift of driving factors for the interannual variability of the winter upper-ocean thermal state near the KE occurred around late-1980s. Because the NPSTMW is highly dependent on the upper-layer thermal states, the same change may exist in the formation of the NPSTMW. However, a recent study by Oka et al. (2019) reported that the variation of the NPSTMW volume is primarily controlled by a remote forcing related with the Pacific Decadal Oscillation with a time lag of 3–4 years using the hydrographic data along the 137°E section from 1967 to 2016. Therefore, the primary driving mechanism for the NPSTMW formation and its potential

nonstationarity is yet to be clarified.

The purpose of this study is to investigate (1) whether there is an epoch-dependent change in driving mechanism of the NPSTMW formation and (2) what causes the epoch-dependent change of the NPSTMW formation. To investigate underlying dynamics and causes of the regime shift for the NPSTMW formation, (1) a long-term (1960–2009) eddy-permitting OGCM forced by the interannual atmospheric forcing and (2) an atmosphere-ocean coupled model (Kiel Climate Model, KCM), which is integrated for 2,000 years under the constant CO_2 concentration at the pre-industrial level, are used in this study. The use of model results will complement the previous studies based on the limited observational data in the study region. It should be noted that the 'regime shift', which is used in this study, is defined as the transition of driving mechanisms for the NPSTMW formation. Therefore, it should be distinguished from the general concept on the regime shift, which is the abrupt changes of the mean state in the climate system.

Chapter 2. Data and methods

2.1 Model description

The global OGCM used in this study is based on the Modular Ocean Model version 4.1 of Geophysical Fluid Dynamics Laboratory. The OGCM solves the primitive equations under Boussinesq and hydrostatic approximation with Arakawa-B grid system (Arakawa & Lamb, 1977). The OGCM has an eddy-permitting grid resolution of 1/4° in both longitudinal and latitudinal directions and 50 vertical levels of z* vertical coordinate (Adcroft & Campin, 2004) with enhanced resolution near the surface. For better representation of the bottom topography, the partial step method (Adcroft et al., 1997; Pacanowski & Gnanadesikan, 1998) is employed to the thickness of bottom cell. A tri-polar grid system (Murray, 1996) is adopted with three poles located at Canada (100°W, 65°N), Russia (80°E, 65°N), and Antarctica to avoid the spherical coordinate singularity at the North Pole. The model topography is derived from the Ocean Circulation and Climate Advanced Modelling project 1/10° bathymetric data set from the Southampton Oceanography Centre. The K-profile parameterization (Large et al., 1994) is used for the vertical mixing. The effect of tidal mixing is parameterized by following the methods of Simmons et al. (2004) and Lee et al. (2006), which consider enhanced vertical mixing due to dissipation of internal tides and bottom friction induced by barotropic tides, respectively. Horizontal viscosity is determined by the Smagorinsky biharmonic scheme (Griffies & Hallberg, 2000) without explicit lateral diffusion. The multidimensional, piecewise method scheme (Colella & Woodward, 1984) and a second-order centered finite difference scheme are applied to calculate the tracer and momentum advection, respectively. Other details of numerical methods in this experiment are based on the oceanic configuration of CM2.5 (Delworth et al., 2012).

The initial condition of the OGCM is set with January-February-March mean temperature and salinity derived from the World Ocean Atlas 2009 (Antonov et al., 2010; Locarnini et al., 2010). The OGCM is spun up over 50 years under the surface heat, freshwater, and momentum fluxes estimated by bulk formula (Large & Yeager, 2004) with the climatological variables of the Coordinated Ocean-sea ice Referenced Experiments phase 2 (CORE2)-Normal Year Forcing (NYF) data set (Large & Yeager, 2009) (Table 1). After the spin-up, the hindcast model is integrated for 61 years from 1949 to 2009 with the annually varying CORE2-Inter-Annual Forcing (IAF) data set (Large & Yeager, 2009). The sea surface salinity is restored to the climatological monthly mean salinity of Polar Hydrographic Climatology (Steele et al., 2001) with a damping timescale of 60 days. It takes about 11 years to reach a stationary equilibrium state for the eddy kinetic energy of upper 400 m in the western North Pacific region. Because the NPSTMW is mainly located in the upper 400 m, last 50 years (1960−2009) will be sufficient to investigate the interannual to decadal variability of the NPSTMW.

The KCM (Park et al., 2009), which is an atmosphere-ocean-sea ice coupled model, is also used to examine the potential ocean-to-atmosphere feedback. The KCM consisting of European Centre for Medium-range Weather Forecasts (ECMWF) Hamburg Atmospheric general circulation Model version 5 (ECHAM5) (Roeckner et al., 2003) as an atmospheric component, and Nucleus for European Modeling of the Ocean (NEMO) (Madec, 2008) as an ocean-sea ice component, with the Ocean Atmosphere Sea Ice Soil version3 (OASIS3) coupler (Valcke, 2006). The atmospheric component has T63 (1.875°×1.875°) horizontal resolution with 22 vertical levels. The oceanic component of KCM has about 0.5° horizontal resolution on a curvilinear grid. There are 46 vertical levels with 19 levels in the upper 500 m. The KCM was integrated for 3,000 years as a pre-industrial simulation employing a constant CO_2 concentration of 286.2 ppm from the Levitus climatology (Levitus et al., 1998). In this study, the last 2,000 years is used to

investigate the variability of the NPSTMW formation after skipping the initial 1,000 years to account for model spin up. More detailed numerical configuration of the KCM can be found in Park et al. (2009).

Table 1. Description of CORE2 surface forcing fields.

Field	Frequency	Units
10 m air temperature	6 hourly	Kelvin degree
10 m specific humidity	6 hourly	kg/kg
10 m zonal wind	6 hourly	m/s
10 m meridional wind	6 hourly	m/s
Sea level pressure	6 hourly	Pa
Downward shortwave	Daily	W/m^2
Downward longwave	Daily	W/m^2
Liquid precipitation	Monthly	kg/m^2/s
Solid precipitation	Monthly	kg/m^2/s
Continental runoff	Annual mean	kg/m^2/s

2.2 Volume budget analysis, statistical methods, and supporting observational data

To quantitatively analyze how the NPSTMW is formed during cooling seasons, the volume budget analysis is conducted using Walin framework (Cerovečki & Giglio, 2016; Guo et al., 2018; Rainville et al., 2007; Walin, 1982). In the Walin framework, the rate of volume change ($\partial V / \partial t$) between two isopycnals (σ_1, σ_2) in a control domain is balanced by the diapycnal volume flux and volume flux through the base of mixed layer, thus the conservation of volume is obtained as follows:

$$\frac{\partial V(\sigma_1 \leq \sigma < \sigma_2, t)}{\partial t} = G(\sigma_1, t) - G(\sigma_2, t) - M(\sigma_1 \leq \sigma < \sigma_2, t), \tag{1}$$

where $V(\sigma, t)$ is the volume of fluid between two isopycnals (σ_1 and σ_2), $G(\sigma, t)$ is the diapycnal volume flux across the isopycnal, and $M(\sigma, t)$ is the volume flux exchange rate (subduction/obduction) between the mixed layer and ocean interior.

The diapycnal volume flux $G(\sigma, t)$ can be derived from a thermodynamic balance of air-sea flux at the surface, and diapycnal diffusive flux across the isopycnal, thus it is given by (Nurser et al., 1999):

$$G(\sigma, t) = F(\sigma, t) - \frac{\partial D(\sigma, t)}{\partial \sigma}, \tag{2}$$

where $F(\sigma, t)$ is transformation rate by air-sea buoyancy flux at the sea surface, and $D(\sigma, t)$ is diapycnal diffusive flux by the mixing across the isopynal surface. The surface transformation rate is determined by the thermal (heat) and haline (evaporation, precipitation) atmospheric forcing, and thereby $F(\sigma, t)$ can be expressed by (Speer & Tziperman, 1992),

$$F(\sigma, t) = -\frac{\partial}{\partial \sigma} \iint_{outcrop} B dA_{surf}, \tag{3}$$

where A_{surf} is the surface density outcrop area between σ_1 and σ_2 isopycnals, and B is the surface buoyancy flux,

$$B(\sigma, t) = -\frac{\alpha Q}{c_p} + \beta \rho S(E - P), \tag{4}$$

where α and β are the thermal expansion and saline contraction coefficients, c_p is the specific heat, Q is the net surface heat flux (negative/positive for ocean heat loss/gain), ρ is the sea surface density, S is the sea surface salinity, E and P are the evaporation and precipitation, respectively. In the KE region, the surface transformation rate term is mainly determined by the thermal (Q) forcing rather than the haline ($E-P$) forcing during cooling seasons (Figure 3 and Figure 4). To sum up, integrating the diapycnal flux ($G(\sigma, t)$) over the outcrop area between two isopycnal surfaces (σ_1, σ_2) yields,

$$G(\sigma_1, t) - G(\sigma_2, t) = \int_{\sigma_1}^{\sigma_2} -\frac{\partial G(\sigma, t)}{\partial \sigma} d\sigma = \int_{\sigma_1}^{\sigma_2} -\frac{\partial F(\sigma, t)}{\partial \sigma} + \frac{\partial^2 D(\sigma, t)}{\partial \sigma^2} \tag{5}$$

$$= -F(\sigma_2, t) + F(\sigma_1, t) + \int_{\sigma_1}^{\sigma_2} \frac{\partial^2 D(\sigma, t)}{\partial \sigma^2} d\sigma.$$
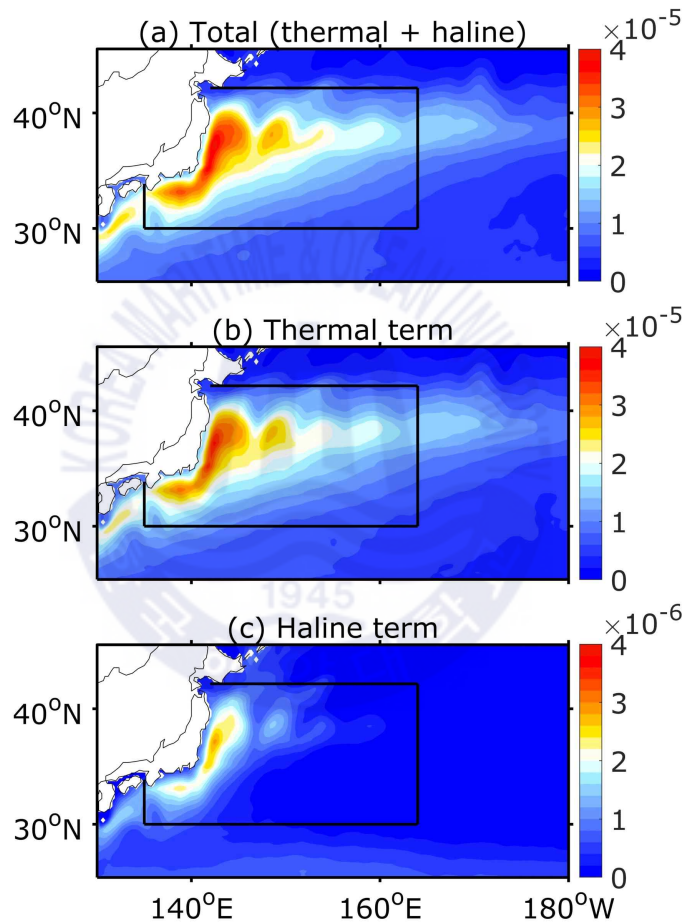
Figure 3. Climatological mean (a) surface buoyancy flux, (b) thermal term, and (c) haline term, which are calculated from the OGCM outputs, during cooling seasons (December to following March).
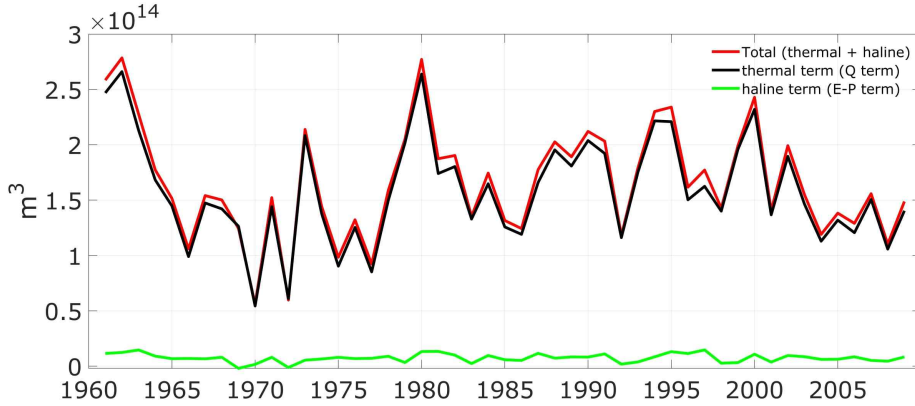
Figure 4. Time series of surface transformation terms integrated during cooling seasons (DJFM). Red, black, and green lines indicate the total (thermal+haline), thermal, and haline terms, respectively.

The subduction/obduction rate (M) is given by (Cushman-Roisin, 1987),

$$M(\sigma_1 \leq \sigma < \sigma_2, t) = \iint_{outcrop_{ml}} d\,dA_{ml}, \tag{6}$$

where d is instantaneous detrainment rate, is A_{ml} is density outcrop area ($\sigma_1 \leq \sigma < \sigma_2$) at the base of mixed layer. The instantaneous detrainment rate (d) is expressed as,

$$d = -\frac{\partial h}{\partial t} - U_h \bullet \nabla h - w_h, \tag{7}$$

where h is the MLD, which is defined by the criterion with the density difference from the depth of 10 m as $\Delta\sigma_\theta = 0.03$ kg m^{-3}, U_h is lateral velocity integrated from the surface to base of mixed layer, w_h is vertical velocity at the base of mixed layer, and A_{ml} is density outcrop area ($\sigma_1 \leq \sigma < \sigma_2$) at the base of mixed layer. The vertical entrainment/detrainment rate term is mainly controlled by the temporal change of the MLD ($\partial h / \partial t$) in the KE region during cooling seasons (Figure 5 and Figure 6).
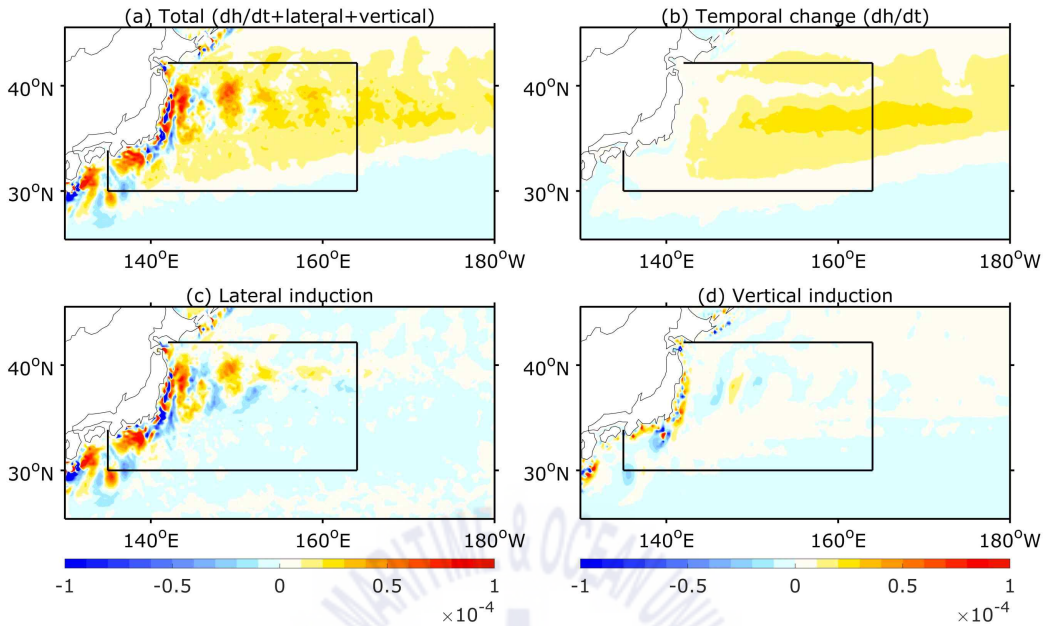
Figure 5. Climatological mean (a) vertical entrainment, (b) temporal change of MLD, (c) lateral induction, and (d) vertical induction terms, which are calculated from the OGCM outputs, during cooling seasons (December to following March).
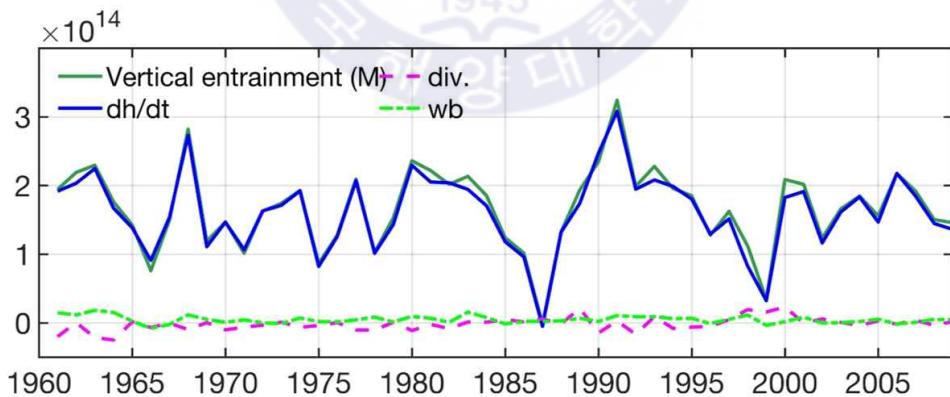
Figure 6. Time series of the vertical entrainment terms (m^3) integrated during cooling seasons (DJFM). Solid green and blue lines indicate the vertical entrainment and temporal change of MLD term, respectively. Dashed purple and dotted green lines denote the lateral and vertical induction terms, respectively.

Following Nishikawa et al. (2013) and Guo et al. (2018), the conservation equation for a control volume (V) bounded by σ_1 and σ_2 isopycnals can be obtained by combining equations (1) and (5),

$$\frac{\partial V}{\partial t} = \int_{\sigma_1}^{\sigma_2} [-\frac{\partial}{\partial \sigma} \iint_{outcrop} -\frac{\alpha Q}{c_p} + \beta \rho S (E-P) dA_{surf}] d\sigma \tag{8}$$
$$-\iint_{outcrop} (-\frac{\partial h}{\partial t} - U_h \cdot \nabla h - w_h) dA_{ml} - \iint \boldsymbol{u} \cdot \boldsymbol{n} dA_{lateral,}$$

where $\boldsymbol{u}$ is the horizontal velocity, $\boldsymbol{n}$ is normal unit vector of the lateral boundary (outward positive), and $A_{lateral}$ is the element of area between σ_1 and σ_2 isopycnals at the lateral surface of four (east, west, south, and north) lateral open boundaries in the analysis domain. It is noted that the advective volume flux, which is the last term of right-hand side of equation (8), is mainly determined by the export through the eastern boundary during cooling seasons (Figure 7). The advective flux through the western boundary is balanced by the flux through the southern boundary. The flux through the northern boundary is almost zero.

The left-hand side of equation (8) is the temporal changes of the control volume; the first, second, and third terms of the right-hand side of equation (8) represent surface transformation rate, vertical entrainment/detrainment rate, and advective volume flux through the lateral boundary in a control domain, respectively. It is noted that the second term of the right-hand side of equation (8) is estimated in the mixed layer for the NPSTMW properties. The isopycnal surface σ_1 and σ_2 are set to lower and upper boundary of NPSTMW density range in each model, respectively. In this study, the rate of volume change ($\partial V / \partial t$), the surface transformation rate (F), the subduction/obduction rate (M), and the lateral advective flux are directly calculated from the model outputs. The diapycnal diffusive flux term (D) is not calculated and included as a part of residual term. It is noted that the equation actually represents the volume budget for the whole water mass of the NPSTMW density range, rather than only the mixed layer portion. Following Guo

et al. (2018), we use the expression of the 'control volume', rather than the 'NPSTMW volume', because the equation (2) does not consider the potential vorticity.
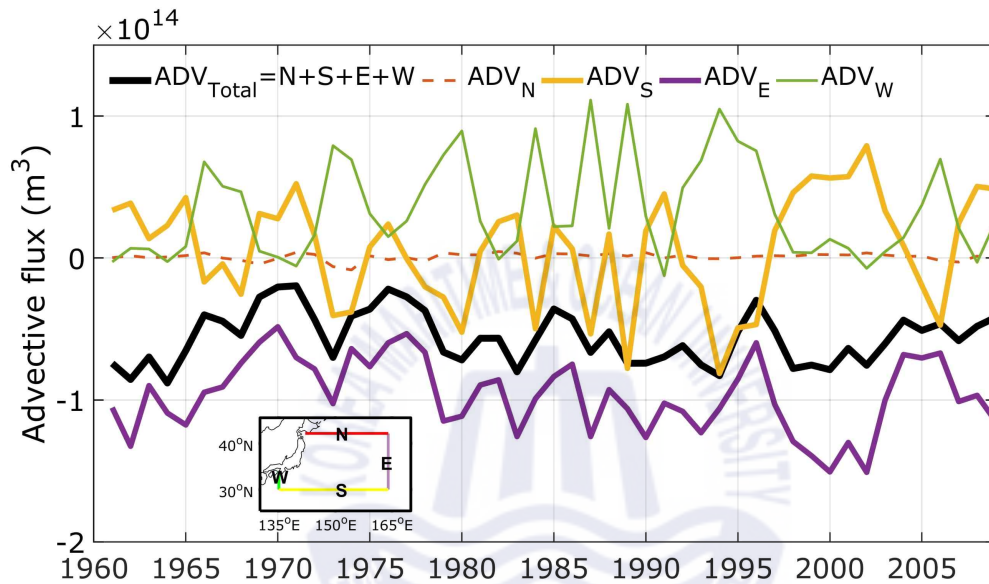
Figure 7. Time series of advective volume flux (I, m^3), which is integrated during cooling seasons (DJFM), through the lateral boundary in a control domain (135−164°E, 30−42°N). Thick black line indicates total advective flux. Solid yellow, purple, and green lines indicate the advective flux through the southern, eastern, and western boundary, respectively. Dashed red line denote the advective flux through the northern boundary.

In order to focus on the formation process of the NPSTMW, equation (8) is integrated over the entire cooling season (December to following March; DJFM), when $\partial V / \partial t$ is positive (i.e., when the control volume increases),

$$\int_{DJFM} \frac{\partial V}{\partial t} dt = ASI + ENT + ADV + Residual, \tag{9}$$

where the left-hand side of equation (9) represents the amount of the volume formation in each cooling season. The terms named as ASI, ENT, and ADV in equation (9) represent the volume formed by the air-sea interaction, vertical entrainment, and advective flux, which can be obtained by time integrating the first, second, and third terms on the right-hand side of equation (8), respectively. The diapycnal diffusive flux is not considered here explicitly; thus, it is regarded as the residual term together with other imbalances including the volume difference between the bottom of mixed layer and the σ_2 density surface. It is noted that the local eddy effect on the NPSTMW formation suggested by Qiu and Chen (2006) did not consider in this study, because the eddy activity in the KE region cannot be reproduced realistically even in the eddy-permitting (1/4°) model.

The statistical significance of the linear regression and the correlation coefficient is estimated by the block bootstrap method (Von Storch & Zwiers, 1999) with 1,000 resamples in blocks of three successive years to reflect the interannual persistence. The moving correlation analysis is conducted to examine the decadal changes of the interannual relationship between the NPSTMW volume and volume budget terms. The bootstrap method is applied for each time segment to determine the statistical significance of the moving correlation. The wavelet analysis and power spectral analysis are also used to examine the periodicity of the time series (Torrence & Compo, 1998). The multivariate regression analysis (Emery & Thompson, 1997) is also used to quantitatively assess the contribution ratio of each volume budget term to the NPSTMW variability.

The performance of the model is validated with the observation-based data sets. The surface current speed is validated with the near-surface current data obtained from Ocean Surface Current Analysis Real-time (OSCAR), derived from the various atmospheric and oceanic observations with 1/3° horizontal resolution from 1998 to

2011. The simulated sea surface height is compared to the 1/4° delayed mode daily absolute dynamic topography distributed by the Archiving, Validation, and Interpretation of Satellite Oceanographic data (AVISO). The simulated PV and the NPSTMW volume are validated with the Argo-derived subsurface PV values provided by Kuroshio Extension System Study (Rainville et al., 2014) and the objective analyses (1° by 1° gridded dataset) of the EN4 dataset (Good et al., 2013), respectively. It is also used the Argo mixed layer climatology and database (Holte et al., 2017), which are interpolated in 1° by 1° grids for 2000−2013.

The CORE2 data set was obtained from https://data1.gfdl.noaa.gov/nomads/forms/core/COREv2.html. The World Ocean Atlas 2009 and the Polar Hydrographic Climatology data set were obtained from https://www.nodc.noaa.gov/OC5/WOA09/pr_woa09.html and http://psc.apl.washington.edu/nonwp_projects/PHC/Climatology.html, respectively. The OSCAR data were taken from https://podaac.jpl.nasa.gov/dataset/OSCAR_L4_OC_third-deg. The database of mixed layer depth is downloaded from http://mixedlayer.ucsd.edu. The data set of the Argo-derived subsurface PV values was taken from http://uskess.whoi.edu/. The sea surface height data observed by the satellite are available from AVISO (http://www.aviso.altimetry.fr/duacs/). The EN4 data set was downloaded from https://www.metoffice.gov.uk/hadobs/en4/.

Chapter 3. Late-1980s regime shift in the formation of the NPSTMW

3.1 Model validation

  The OGCM reproduces strong surface currents along the Kuroshio path and major features of the KE such as the realistic quasi-stationary meanders (Figures 8a and 8b). However, compared with the OSCAR, there is an overshooting of the Kuroshio, which is a common feature in the eddy-resolving OGCM simulation (Masumoto et al., 2004) and even in the non-eddy-resolving OGCM simulation (Xu et al., 2014). In the observation, there are two separated regions showing deep MLD (>150 m) located south of Kuroshio (140−160°E, 30−35°N) and downstream region of Oyashio Extension (160°E−180°, 35−42°N) (Figure 8c). The OGCM well reproduces those deep MLD regions, although the separation into the two regions is not such clear (Figure 8d). This is also believed to be a common limitation of eddy-permitting OGCM simulations (Toyoda et al., 2004; Tsujino & Yasuda, 2004). In this study, the deep MLD region (>100 m) near KE is considered as the main formation area of the NPSTMW and a study region (135−164°E and 30−42°N; box in Figures 8b and 8d). Even if the target domain is shifted by several degrees from the study region, the results of the subsequent analyses are still robust. The domain defined here is a few degrees north of that in the observations (Cerovečki & Giglio, 2016: 20−40°N; Qiu & Chen, 2006: 31−38°N) due to the overshooting of the Kuroshio in the OGCM.
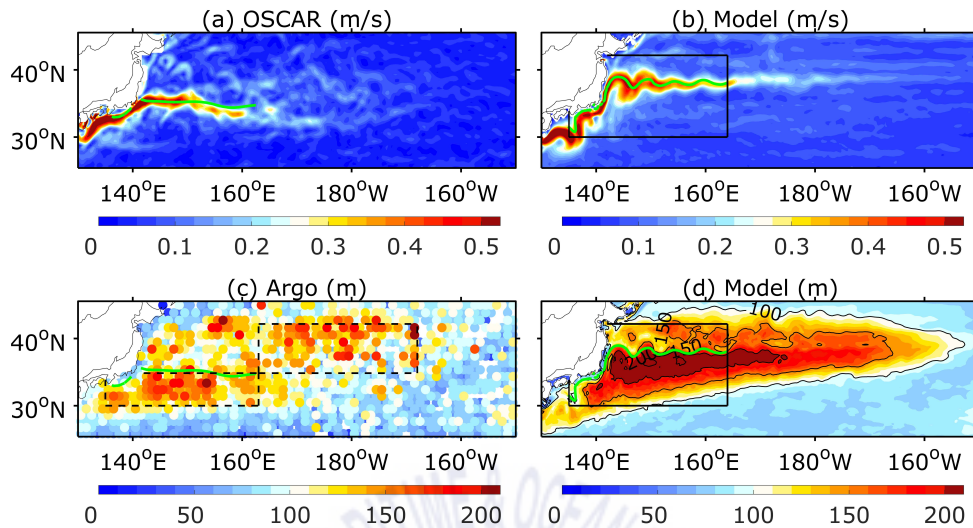
Figure 8. Climatological mean sea surface current speed (m s^{-1}) for (a) the observation (OSCAR, 1998−2011) and (b) the OGCM (1998−2009) during the cooling seasons (December to following March). Mixed layer depth (m, $\Delta\sigma_\theta = 0.03$ kg m^{-3}) from (c) the Argo observation (2000−2013, Holte et al., 2017) and (d) the OGCM (2000−2009) during the cooling seasons. Green lines indicate the Kuroshio main axis defined as the 12°C isotherm at the depth of 300 m from (a,c) the World Ocean Atlas 2009 and (b,d) the OGCM. Dashed-line boxes in (c) indicate the formation area of the North Pacific subtropical mode water and central mode water (Kobashi et al., 2006; Oka & Qiu, 2012). Box in (b) and (d) indicates the study region in this study.

Figure 9 shows the temporal evolution of the SSH anomaly, which represents the KE variability (Qiu & Chen, 2014). It should be noted that the latitude bands of the analysis area are set as 33−38°N for the OGCM and 31−36°N for the observation considering the overshooting of the Kuroshio in the OGCM. The OGCM reproduces well the temporal variation of the SSH in the KE region compared to the observed one from 1993 to 2009 ($r = 0.82$), though there are

some differences in the magnitude of the SSH anomaly. During the total analysis period (1960−2009), there are distinct interannual and decadal variability in the SSH anomaly. It is intriguing that the variability period is changed after 1980s; the decadal variability is obvious after 1980s.
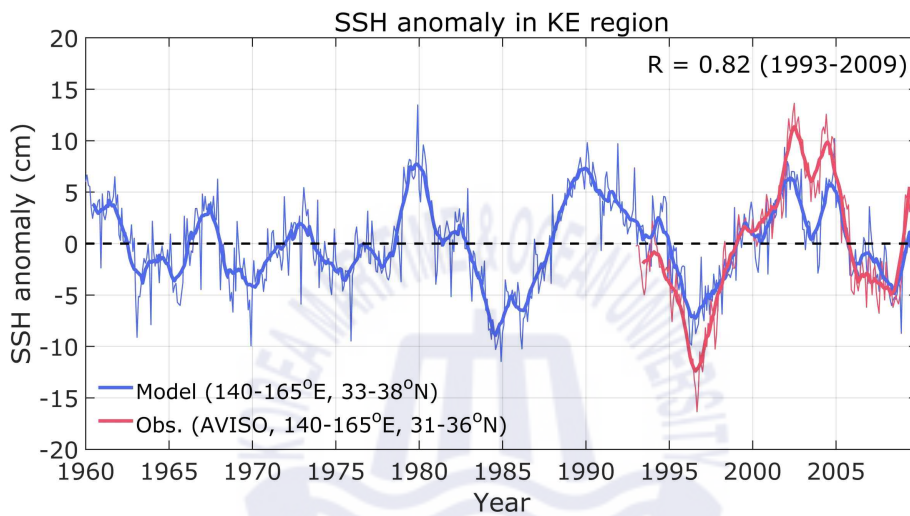
Figure 9. Time series of the SSH anomaly in the KE region (140°−165°E. 31°−36°N for the observed one from the AVISO and 140°−165°E. 33°−38°N for the OGCM). Thin red and blue lines indicate the OGCM and the observation, respectively. Thick lines indicate the 12-month moving average values.

To validate the simulated NPSTMW in the formation area, the domain-averaged PV of the OGCM is compared with that in the Argo observation during the period of 2001−2009 (Figure 10). The PV is defined as

$$PV = -\frac{f}{\rho_0}\frac{\partial \rho}{\partial z}, \tag{10}$$

where f is the Coriolis parameter. ρ_0 and ρ are the mean (1,025 kg m^{-3}) and anomalous potential density of seawater, respectively. The low PV water is formed

when the mixed layer gets deep during cooling season (December to following March) in both the simulation and observation. It is trapped below the seasonal thermocline during the warming season (April to August) and finally reemerged to the sea surface in the following December, which is so-called the reemergence process of the NPSTMW (Figure 2; Alexander et al., 1999; Sugimoto & Hanawa, 2005). Although there is an overshooting of the Kuroshio, the interannual evolutions of the low PV water in the OGCM and the Argo observation are very similar (Figure 10). Therefore, the long-term OGCM result can be used for investigating the variability of the NPSTMW formation over the longer period, in which the Argo data do not exist.
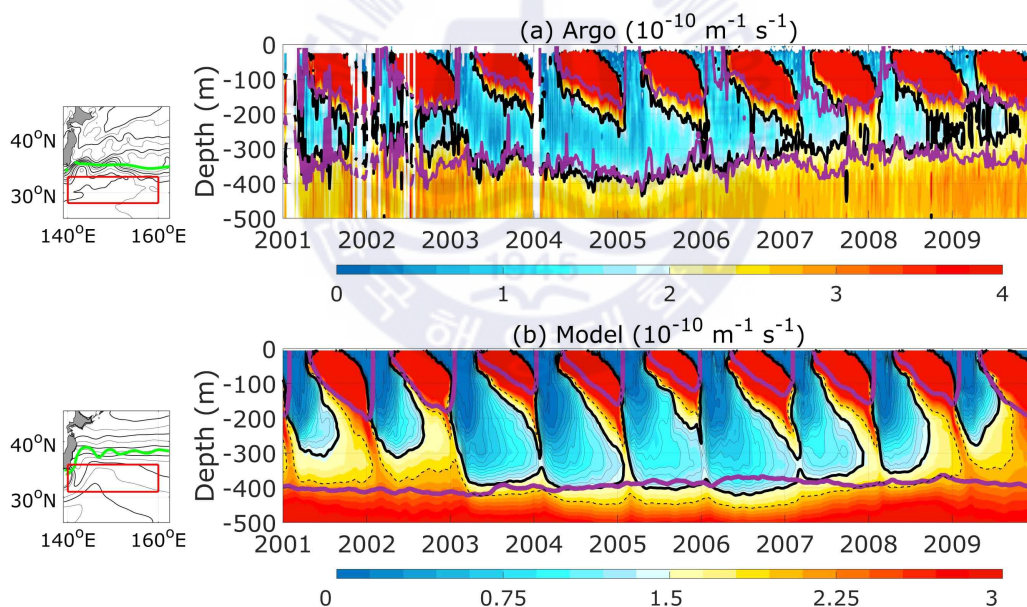
Figure 10. The depth-time sections of the domain average potential vorticity (PV) from five-daily mean data from (a) the Argo floats and (b) the OGCM. The analysis domains are 140−160°E, 28−33°N for the observation and 140−160°E, 31−36°N for the OGCM (red boxes in the thumbnail maps). Thick black contours indicate PV = 2.0 × 10^{-10} m^{-1} s^{-1} for the observation and PV = 1.5 × 10^{-10} m^{-1} s^{-1}

for the OGCM. Thin dashed lines denote PV = 2.0 × 10^{-10} m^{-1} s^{-1} for the OGCM. Solid purple lines indicate the isopycnal layers of σ_θ = 25.0, 25.5 kg m^{-3} for the observation and σ_θ = 25.1, 25.7 kg m^{-3} for the OGCM. Blanks in (a) indicate that the Argo data do not exist over 5 days in the analysis area. In the thumbnail maps, time mean sea surface height is contoured every 10 cm from the AVISO observation and the OGCM during the corresponding years. Green lines in the thumbnail maps indicate the 12°C isotherm at the depth of 300 m representing the Kuroshio main axis from the World Ocean Atlas 2009 and the OGCM.

The NPSTMW is defined as a potential density anomaly (σ_θ) range of 25.1−25.7 kg m^{-3} and the low PV (<1.5 × 10^{-10} m^{-1} s^{-1}) conditions. It is followed Xu et al.'s (2014) threshold of the low PV, which is stricter PV criterion (PV < 1.5 × 10^{-10} m^{-1} s^{-1}) in the OGCM simulation, smaller than the typical value (PV < 2.0 × 10^{-10} m^{-1} s^{-1}) applied to observation, because the low-PV water volume (PV < 2.0 × 10^{-10} m^{-1} s^{-1}) is overestimated in the OGCM (dashed line in Figure 10b) due to the overshooting of the Kuroshio in the OGCM. The stricter PV criterion constrains the simulated NPSTMW volume to be consistent with the observation using typical threshold (Figure 10). Additionally, the minimum thickness of the NPSTMW was set to 50 m following Douglass et al.'s (2012) suggestion. The volume of NPSTMW is estimated by multiplying the thickness (h) of NPSTMW by the grid size ($dx \times dy$) in each grid cell. In this study, the interannual variations of the NPSTMW volume are represented by its time series in March, when the volume of the NPSTMW becomes its maximum value (Figure 11; Rainville et al., 2014; Suga & Hanawa, 1990).
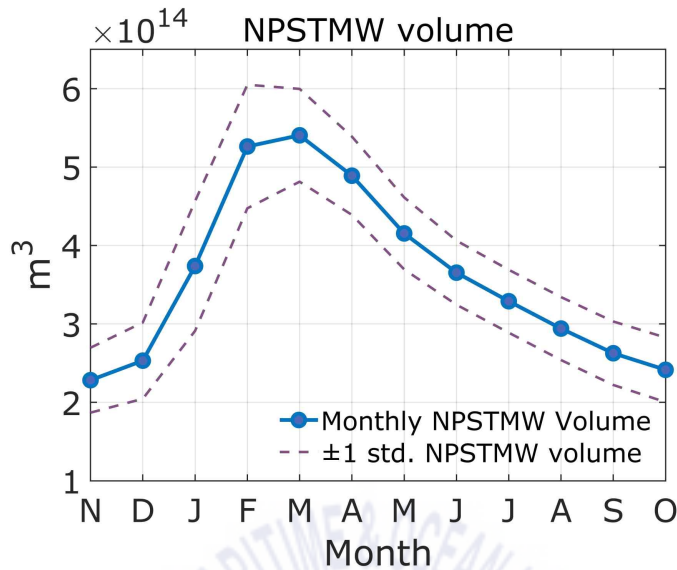
Figure 11. Time series of the monthly mean NPSTMW volume.

To check the model performance for the long-term variation of the NPSTMW volume, the potential vorticity is compared with the NPSTMW volume for the period of 1960−2009 with the EN4 data (Figure 12). It is noted that the NPSTMW of the EN4 is defined by a potential density anomaly range between 25.0 and 25.5 kg m^{-3} with the low PV ($< 2.0 \times 10^{-10}$ m^{-1} s^{-1}) conditions, which is applied to the observation (Rainville et al., 2014). In the EN4, the formation of the low PV water increases (decreases) in early 1980s, 1990s, and mid-2000s (mid-1980s, 1990s, and late-2000s) (Figure 12a). The OGCM appears to reproduce well such increase and decrease of the low PV water formation in the same periods (Figure 12b). Although there are some discrepancies between the OGCM and EN4 due to the different definition of the NPSTMW, both time series shows quite similar evolution of the NPSTMW volume ($r = 0.6$, Figure 12c). For example, the decadal variability of the NPSTMW volume shows a small (large) variation before (after) 1990.
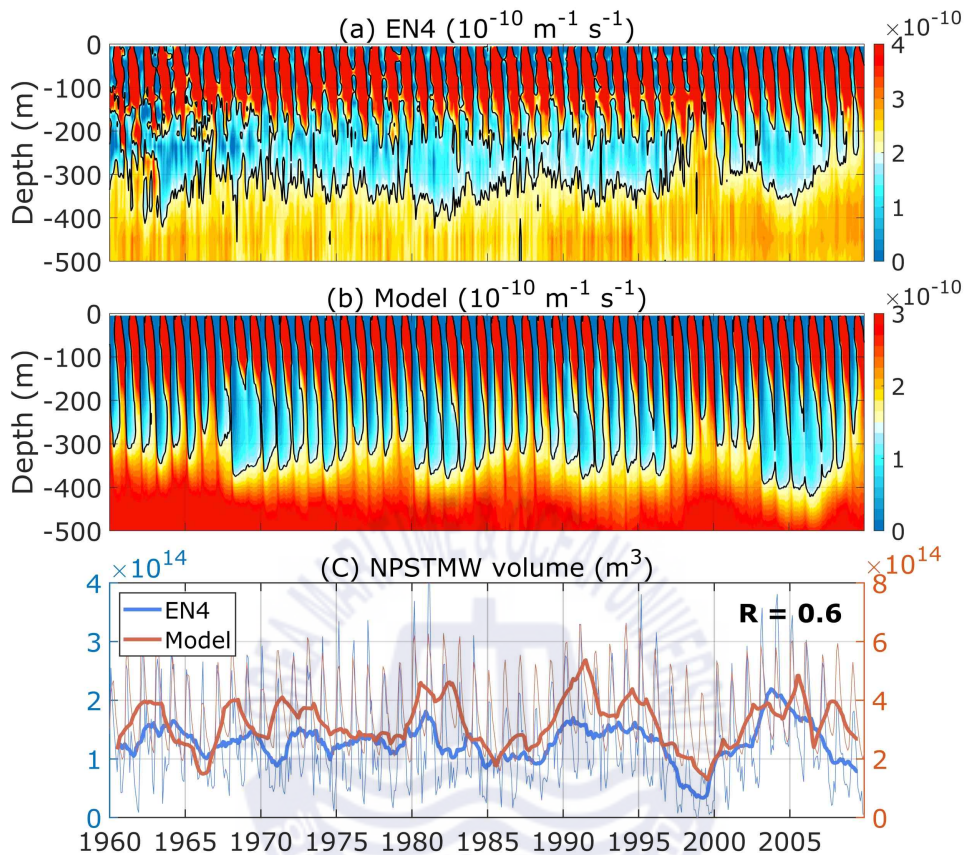
Figure 12. The depth-time sections of the domain average potential vorticity (PV) from (a) the EN4 and (b) the OGCM. The analysis domains are 140−160°E, 28−33°N for the observation and 140−160°E, 31−36°N for the OGCM. Thick black contours indicate PV = 2.0×10^{-10} m^{-1} s^{-1} for the obervation and PV = 1.5×10^{-10} m^{-1} s^{-1} for the OGCM, respectively. (c) Time series of the NPSTMW volume of the EN4 (blue) and the OGCM (red). Thick lines indicate the 12-month moving averaged NPSTMW volume.

3.2 NPSTMW formation and its variability

To quantitatively analyze how the NPSTMW is formed during winter, the volume

budget is estimated with equation (9) in the formation area of the NPSTMW. It is notable that the ASI (1.65×10^{14} m^3) and the ENT (1.85×10^{14} m^3) terms dominate the formation of the density class for the NPSTMW during 1961−2009 (2.11×10^{14} m^3) (Figure 13). On the other hand, the ADV (−0.88×10^{14} m^3), which is dominated by the advection through the eastern boundary of the domain, shows a minor loss with limited variability. Also, the residual (−0.51×10^{14} m^3) term acts to lose the volume of the NPSTMW. This result is consistent with the findings by Rainville et al. (2007) and Cerovečki and Giglio (2016) based on observations.

Strong interannual variability is observed in the time series of the volume budget terms, especially in the NPSTMW volume in March (blue line in Figure 14) and DJFM integrated formation ($\partial V / \partial t$) term (black line in Figure 14). Both time series show a similar temporal evolution during 1960−2009. Although the volume budget terms are calculated without imposing the low PV constraint, the annual formation amount of the NPSTMW density class in the volume budget is highly correlated with the NPSTMW volume in March, which is estimated with the PV constraint ($r = 0.71$) (Figure 14). This result indicates that the non-PV volume budget terms in equation (9) can be used to assess how much each term contributes to the interannual variability of the NPSTMW volume in March. Therefore, the other budget terms (right-hand side of equation (9)) along with the NPSTMW volume in March is adopted to explain the contribution of the ASI and the ocean dynamics to the interannual variability of the NPSTMW volume.
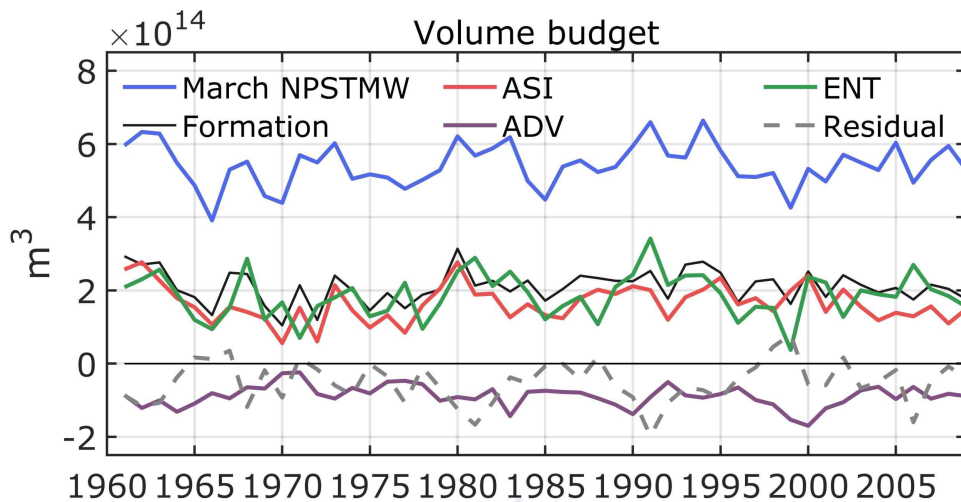
Figure 13. Time series of volume of the NPSTMW in March (blue) and volume budget terms of equation (9). Volume budget terms integrated during cooling seasons (DJFM) include volume formation (black), air-sea interaction (ASI, red), advection (ADV, purple), vertical entrainment (ENT, green), and residual (dashed gray) terms.
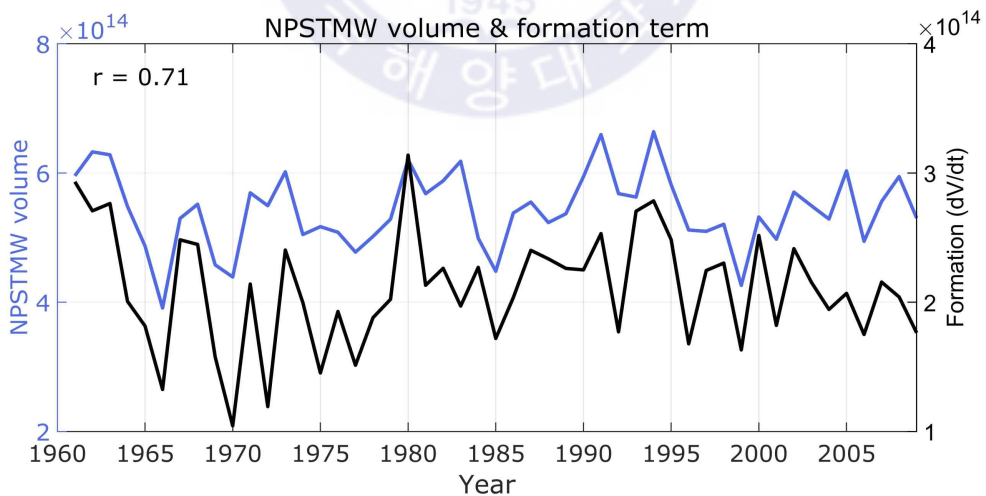
Figure 14. Time series of NPSTMW volume in March (blue) and volume formation term (*dV/dt*, black).

To investigate the contribution of the atmospheric and oceanic forcing on the NPSTMW formation, the formation terms in equation (9) is divided into two: local ASI and ocean dynamics. Here, ocean dynamics terms contain ENT and ADV terms in equation (9). Considering the mixed layer heat budget analysis, the ENT can be related with the ASI, because the ENT is also affected by the surface heat flux. However, it is noted that the ENT has no significant correlation with the ASI (figure 15), and thereby the ENT reflects primarily the ocean dynamics as its correlation with the ASI term is limited (r = 0.27) in the NPSTMW volume budget analysis. Furthermore, it is also noted that the ENT term is more dominant over the ADV term in terms of the interannual variability of the ocean dynamics term (Figure 13).
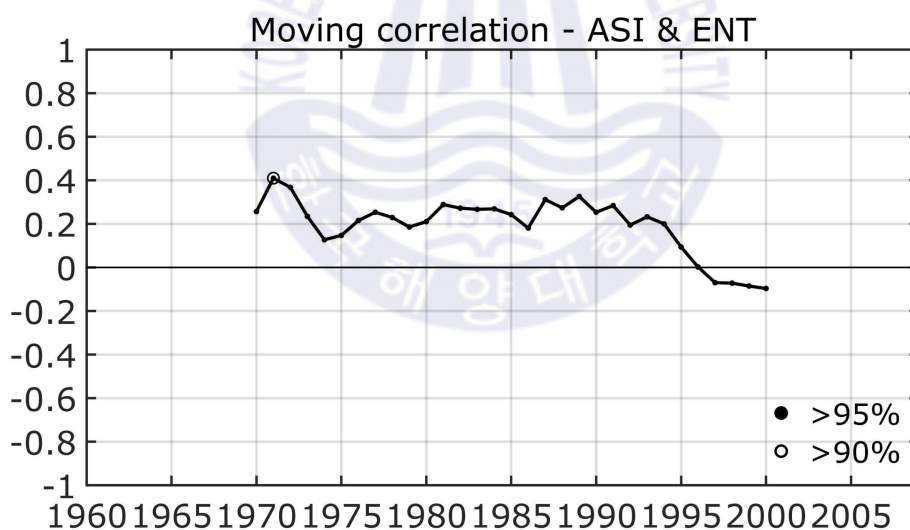
Figure 15. The 21-year moving correlation coefficient between the ASI and the ENT terms. Closed and open circles indicate significant correlation coefficients at the 95% and 90% confidence level, respectively. The 21-year moving correlation is the correlation between two time series within the window of ±10 years relative to the corresponding year.

To look into the change of driving factors for the NPSTMW formation, it is calculated 21-year moving correlation coefficients between the NPSTMW volume and formation terms in equation (9) (Figure 16a). It is notable that there is a sudden change of the driving mechanism for the interannual variability of the NPSTMW volume around late-1980s. Before the period around late-1980s, the local ASI term is significantly correlated with the NPSTMW volume in March at 95% confidence level, while ocean dynamics terms have no significant correlation with it before early-1980s. Since late-1980s, the ocean dynamics exhibits a significant correlation with the NPSTMW volume at 95% confidence level, but the local ASI term does not. This is supported by the 21-year moving standard deviations of volume budget terms (Figure 16b) showing the increase (decrease) of the variability of the ocean dynamics (ASI) term after the late-1980s.

The results are robust regardless of the moving window length between 13 and 23 years (Figure 17). The decadal change of the formation mechanism of the NPSTMW is also consistent with previous studies showing the winter regime shift of upper-layer thermal states around KE region (Pak et al., 2014, 2019; Park et al., 2012; Sugimoto & Kako, 2016). Considering the contrasts of the two moving correlation coefficients in Figure 16a, the total analysis period is separated into two distinct 21-year epochs, 1962−1982 and 1988−2008.

To quantitatively analyze the contribution of the ASI and the ocean dynamics, especially the ENT term, on the variability of the NPSTMW, the multivariate regression analysis is conducted as $Z = aX + bY + \varepsilon$, where Z, X, and Y are the normalized anomaly of the NPSTMW volume in March, ASI, and ENT, respectively (Figure 18). It is again noted that the correlation between X (ASI) and Y (ENT) is insignificant ($r = 0.27$) each other (Figure 15). The relative contribution ratio is determined as $a/(a + b)$ and $b/(a + b)$ by using two regression coefficients a and b. During 1962−1982, the ASI has a dominant influence on the NPSTMW ($a/(a + b) = 0.71$), explaining 57.1% of total NPSTMW variance, compared to that

of the ENT ($b/(a + b) = 0.29$). On the other hands, the contribution of the ENT (ASI) on the NPSTMW dramatically increases (decreases) by $b/(a + b) = 0.88$ ($a/(a + b) = 0.12$), explaining 36.0% (almost 0%) of total NPSTMW variance during 1988−2008. These results suggest that the variability of the NPSTMW is mainly controlled by the ASI (ENT) during 1962−1982 (1988−2008).
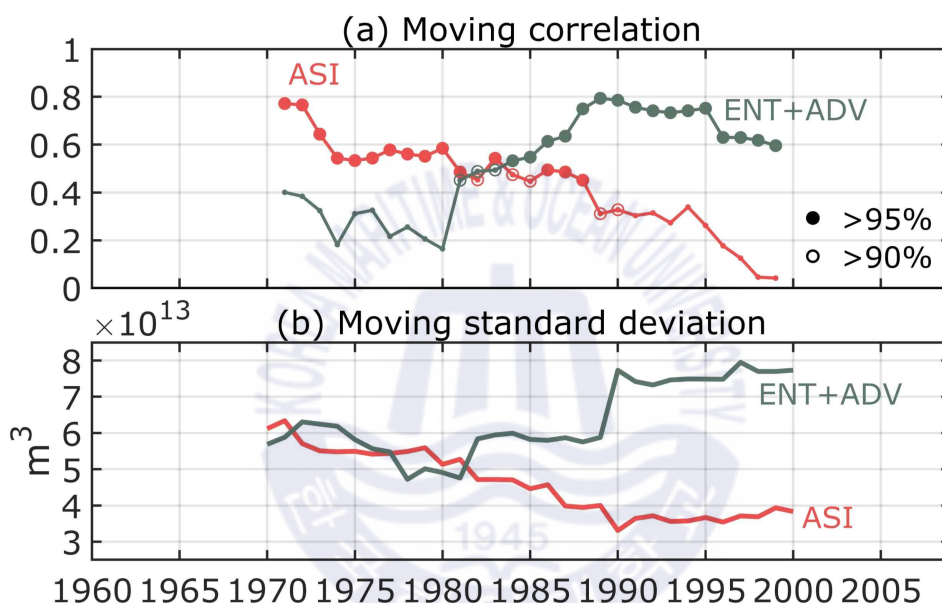
Figure 16. (a) The 21-year moving correlation coefficient of the NPSTMW volume in March with the air-sea interaction (red) and the ocean dynamics (vertical entrainment and advection, cobalt green) terms. Closed and open circles indicate significant correlation coefficients at the 95% and 90% confidence level, respectively. The 21-year moving correlation is the correlation between two time series within the window of ±10 years relative to the corresponding year. (b) The 21-year moving standard deviation of the air-sea interaction (red) and the ocean dynamics (cobalt green) terms.
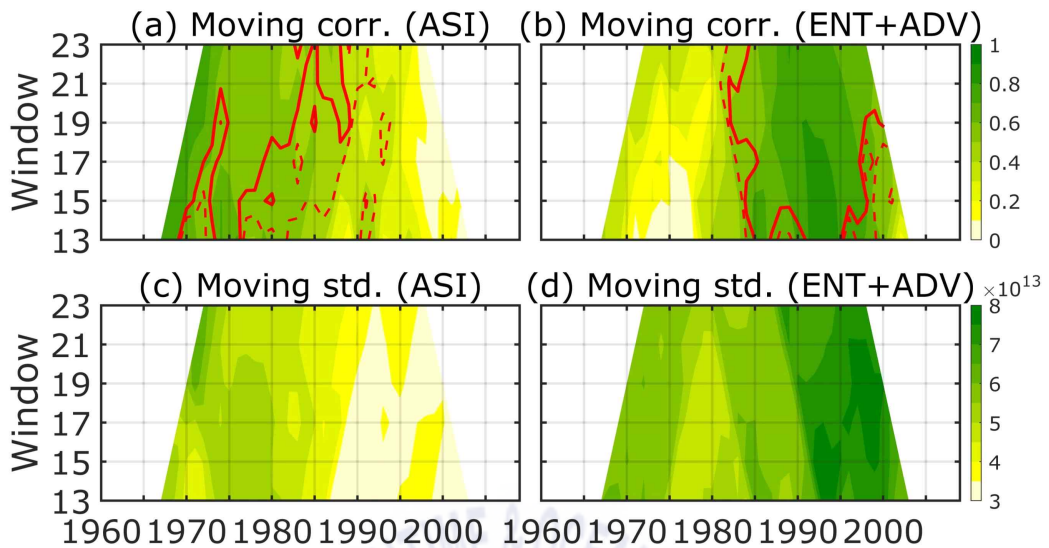
Figure 17. (a) Moving correlation coefficients between the NPSTMW volume in March and the ASI term with the window size between 13 and 23. Solid and dashed red lines indicate significant correlation coefficients at the 95% and 90% confidence level, respectively. (b) As in (a), but for the ocean dynamics term (ENT+ADV). (c,d) Moving standard deviation of the (c) ASI term and (d) the ocean dynamics (ENT+ADV) terms with the window size between 13 and 23.
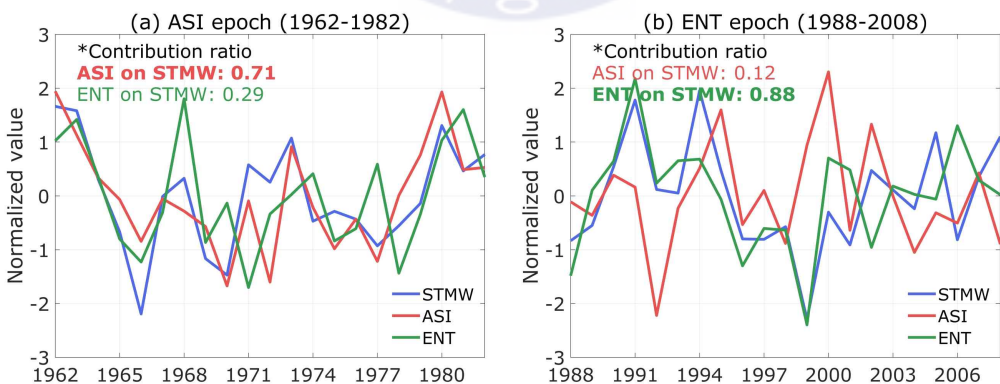
Figure 18. (a) Normalized anomalies of the NPSTMW volume in March (blue), ASI (red), and ENT (green) terms during ASI epoch (1962−1982). (b) Same as in

(a), but for during the ocean dynamics epoch (1988–2008).

3.3 Relationship between NPSTMW and basin-scale climate variability

The dynamical and thermodynamical processes in the KE region are greatly affected by the local and lagged remote influences of the basin-scale climate variability (Kwon et al., 2010). Therefore, large-scale climate variability in the North Pacific can be a key to explain the interannual variability of the NPSTMW formation. To quantify the interannual variability of the atmospheric forcing, the two leading empirical orthogonal functions (EOFs) of the DJFM mean sea level pressure (SLP) anomaly is analyzed from the CORE2-IAF in the North Pacific (120°E–120°W, 20–60°N) during 1960–2009 (Figure 19). The SLP anomaly is weighted by $(\cos\theta)^{1/2}$ to consider the meridionally varying grid size by following the method of Linkin and Nigam (2008). The first and second loading vectors of the SLP resemble the Aleutian Low (AL) pressure pattern (Trenberth & Hurrell, 1994) and the North Pacific Oscillation (NPO) pattern (Linkin & Nigam, 2008), respectively. The second PC (PC-2) is considered as the NPO index (Yeh et al., 2018).
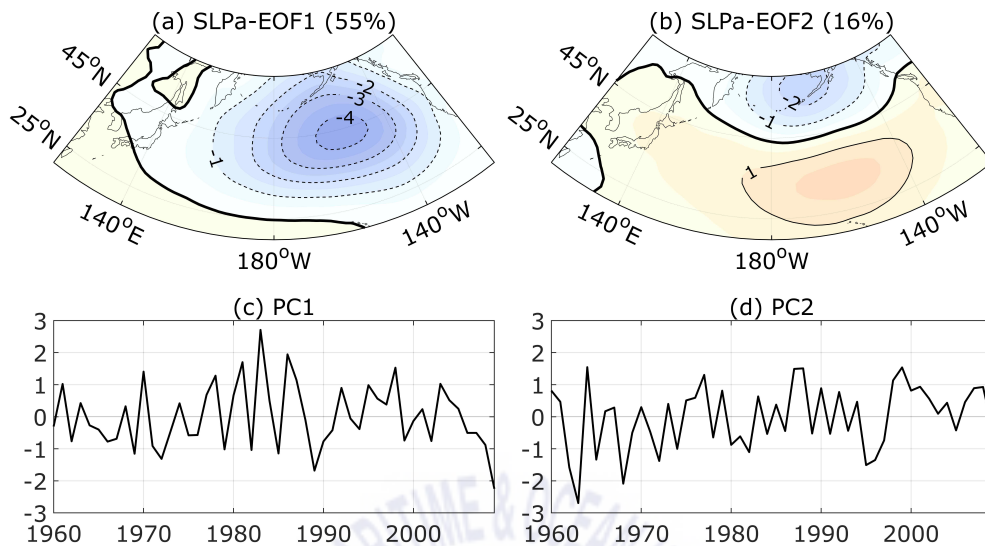
Figure 19. (a) First and (b) second EOFs of the DJFM mean sea level pressure anomaly during 1960−2009 over the North Pacific region (120°E−120°W, 20−60°N). (c-d) PC time series for the (c) first and (d) second EOFs of the SLP anomaly.

Comparing the March NPSTMW volume time series with the leading PC times series of basin-scale SLP, it is found the significant relationship between the NPSTMW volume in March and the NPO index during the whole analysis period (Figure 20a). The NPO has marginally significant correlation with the NPSTMW volume ($r = -0.29$), and the correlation coefficient between the PC-1 and the NPSTMW volume is insignificant ($r = 0.11$). More importantly, the lag correlations between the NPO index and the NPSTMW volume in March show that the NPO exhibits a statistically significant correlation with the NPSTMW volume at different time lags in the two periods (Figures 20b and 20c).

During the period of 1962−1982, the NPO index is concurrently correlated with the volume of the NPSTMW in March (Figure 20b; $r = -0.46$). Note that there is no significant correlation, when the NPO index leads the NPSTMW volume. It

implies that the interannual variability of the formation of the NPSTMW is related to the simultaneous atmospheric forcing associated with NPO in this period. This is consistent with Pak et al. (2014) who showed that the winter SST variability in the western North Pacific is under the influence of the mutually correlated EAWM and NPO patterns before the 1987/1988 regime shift. Due to the interannual variability of the atmospheric condition is strong in the western North Pacific during the former period (Pak et al., 2014, 2019), the NPSTMW volume variability is likely dominated by local air-sea interaction. This is consistent with the volume budget analysis showing the stronger variability of the ASI term during the former period (Figure 16b).

During the period of 1988−2008, the correlation coefficient between the NPO index and the NPSTMW volume in March is maximum (r = 0.51), when the NPO leads by 4 years (Figure 20c). The 4-year lag is consistent with the first mode baroclinic Rossby wave propagation timescale from the central North Pacific to reach the KE region (Qiu & Chen, 2010; Sugimoto & Hanawa, 2010), where the NPSTMW is mainly formed. Sugimoto and Hanawa (2010) reported that the AL activity related to the West Pacific (WP) teleconnection pattern (Barnston & Livezey, 1987; Wallace & Gutzler, 1981), which is upper-level expression of the NPO, influences the formation of the NPSTMW by affecting the main thermocline depth variations in the central North Pacific via the westward Rossby wave propagation. When the NPO is positive, the deeper thermocline propagated from the central North Pacific can be a precondition for the deeper MLD in the formation area of the NPSTMW and, in turn, increase the NPSTMW formation. On the other hand, the simultaneous correlation coefficient between the NPO and the NPSTMW volume gets insignificant, suggesting that the local atmospheric forcing associated with NPO has minor influence on the NPSTMW variability (Figure 20c).
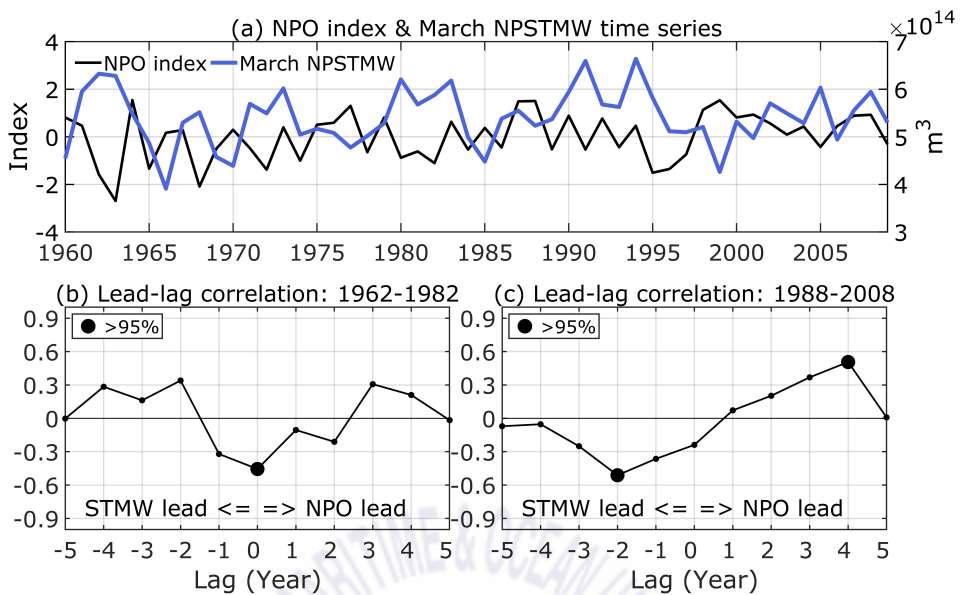
Figure 20. (a) Time series of the NPO index (empirical orthogonal function PC-2 of sea level pressure anomaly) (black) and the NPSTMW volume in March (blue). (b,c) Lead-lag correlation between the NPO index and the NPSTMW volume in March during (b) 1962−1982 and (c) 1988−2008. Positive lag indicates that NPO index leads the NPSTMW volume. Black circle indicates significant values at the 95% confidence level.

The Hovmöller diagram for the anomalies of DJFM $\sigma_\theta = 25.7$ kg m^{-3} (here after $25.7\sigma_\theta$) isopycnal surface depth, which corresponds to the lower boundary of the NPSTMW, between 33°N and 37°N supports the presence of the westward wave propagation during the later period (Figure 21a). Although the isopycnal of $25.7\sigma_\theta$ does not include the PV criterion, its temporal evolution is quite similar with that of the vertically averaged PV anomaly in the NPSTMW isopycnal layer as reported by Cerovečki and Giglio (2016) (see their figures 15 and 16). The latitude band 33−37°N is adopted to consider the model bias due to the Kuroshio overshooting. Even if the target domain is shifted by several degrees in the latitudinal direction compared to the observational analyses by Cerovečki and Giglio (2016), the results

are comparable.

After 1990, the Hovmöller diagram shows the westward propagation signal of the anomalies of $25.7\sigma_\theta$ isopycnal surface depth over 3−4 years from the central North Pacific. Due to the limitation of the eddy-permitting horizontal resolution (1/4°), the feature of the westward Rossby wave propagation and the associated eddy field is somewhat different compared to that of the observation (Fig. 4b of Qiu et al., 2007). Despite of this limitation, the zonally averaged $25.7\sigma_\theta$ isopycnal depth between 160°E and 180° exhibits significant maximum correlation with that between 140°E and 145°E when the former leads by 4 years during 1988−2008 ($r = 0.45$) (Figure 21b). This lag correlation suggests a delayed response of the NPSTMW volume to the anomalies of $25.7\sigma_\theta$ isopycnal depth in the central North Pacific. The westward propagating speed is about 3.2 cm s^{-1}, which is very similar to that estimated by Qiu and Chen (2010) (3.7 cm s^{-1}) in the latitude 32−34°N band based on the satellite altimeter. On the contrary, during the former period, the westward propagation is not clear ($r = -0.28$) (Figures 21a and 21b).
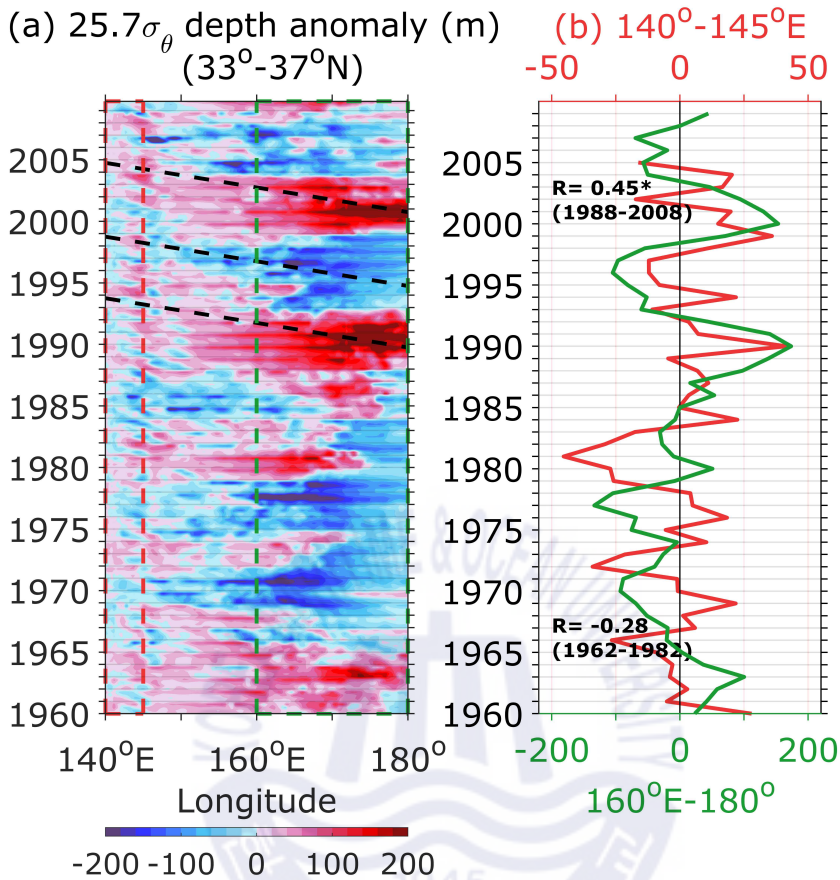
Figure 21. (a) The time-longitude Hovmöller diagram of DJFM $\sigma_\theta = 25.7$ kg m^{-3} isopycnal surface depth anomaly, which is meridionally averaged between 33°N and 37°N during 1960−2009. The thick dashed line indicates the westward propagating $\sigma_\theta = 25.7$ kg m^{-3} isopycnal surface depth anomaly. (b) Comparison between DJFM mean depth anomaly of $\sigma_\theta = 25.7$ kg m^{-3} isopycnal surface averaged in central North Pacific region (160°E−180°, 33−37°N, green) and that of western North Pacific region (140−145°E, 33−37°N, red). The time axis of western North Pacific region (black line) is shifted −4 years to highlight the lagged relationship between two time series. Asterisk mark indicates statistically significant at the 90% confidence level.

Note that there is a hint of ocean-to-atmospheric feedback when NPSTMW leads

NPO by 2 years during 1988−2008 (Figure 20c), which is consistent with Ceballos et al. (2009, see their figure 3b), who mentioned the self-sustained oscillation between the ocean and atmosphere. However, in this study, it is focused only on the response of the NPSTMW to the climate variability. The correlation coefficients between the SLP PC-1 and the volume of the NPSTMW in March (Figure 22) is also calculated. While the correlation is not statistically significant for the entire period or the early period (1962−1982), it becomes significant ($r = -0.52$) during the period of 1988−2008 when the SLP PC-1 leads by 1 year. This result may be consistent with that of Na et al. (2018), who showed that the variability of the meridional movement of the KE-subarctic frontal zone is strongly correlated by 1-year lag to the Pacific Decadal Oscillation, while the variability of the KE strength is related to the North Pacific Gyre Oscillation by 4-year lag. The fast response by 1 year of the NPSTMW volume may be associated with a barotropic response to the Pacific-North American (PNA) teleconnection pattern-like variability, though further analysis will be carried out to reveal this relationship.

(a) SLPa PC1 & March NPSTMW time series

(b) Lead-lag correlation: 1962-1982

(c) Lead-lag correlation: 1988-2008
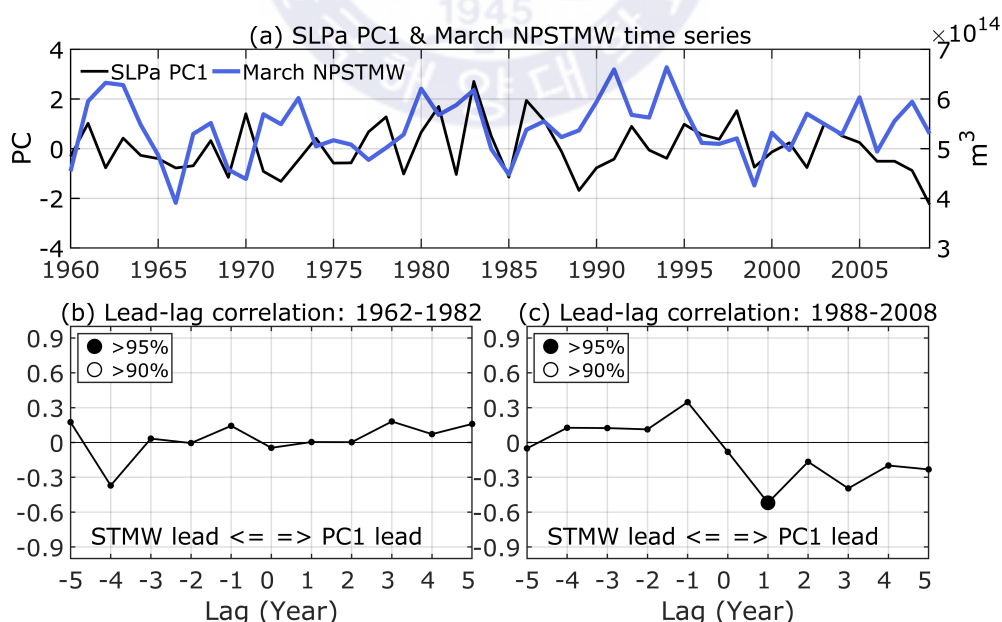
Figure 22. As in Figure 4, but for the EOF PC-1 of sea level pressure anomaly.

3.4 Possible reasons for regime shift in the NPSTMW formation

According to the preceding section, one of the key differences between the two contrasting epochs is the presence of the Rossby wave propagation from the central North Pacific to the NPSTMW region. First of all, the epoch-dependent presence of the Rossby wave propagation can be attributed to the suppression due to the strong local atmospheric variability. In addition, the remote forcing may have been much weaker (stronger) to begin with during the former (later) period. The zonal distribution of the wind stress curl (WSC) is examined to investigate the local and remote WSC forcing in two contrasting periods. Figure 23a shows the Hovmöller diagram of the DJFM WSC (estimated from the input wind fields) meridionally averaged between 33°N and 37°N, which corresponds to the main formation area of the NPSTMW. The most noticeable difference between the two epochs is the zonal location of the largest WSC anomalies. Prior to the late-1980s, the WSCs are overall zonally uniform over 140°E–180°, and the largest positive anomalies are found in the NPSTMW formation region (145–155°E). On the other hand, after late-1980s, the sign of the large WSC around the dateline is generally opposite to the weaker anomalies near the formation area of the NPSTMW (140–160°E).

More importantly, the thermocline anomalies produced by the large WSC anomalies in the central North Pacific 4 years prior are not opposed by the large positive WSC anomalies in the NPSTMW formation region, as they propagate westward via Rossby wave, since late-1980s. Therefore, the large remote WSC anomalies can effectively influence the formation of the NPSTMW (Qiu et al., 2014). Conversely, the effect of weaker remote WSC anomalies on the thermocline during the early period is often opposed by larger local WSC anomalies in the NPSTMW formation region; thus, the zonally uniform WSC distribution during the

former period is not favorable to produce the propagating Rossby waves (Figure 23a).

The epoch-dependent role of the remote and local WSC distributions is further supported by their respective correlation with the NPSTMW volume (Figure 23b). The zonal averages of the WSC between 145°E and 155°E show significant simultaneous correlation with the NPSTMW volume in March during 1962−1982 (r = 0.54), while the impact of the local WSC on the NPSTMW is not significant during 1988−2008 (r = 0.14; Figure 23b). On the other hand, the zonal averages of the WSC between 160°E and 180° show significant 4-year leading correlation with the NPSTMW volume in March during 1988−2008 (r = −0.46; Figure 23b), suggesting the delayed response of the NPSTMW volume to the WSC in the central North Pacific. Also, the corresponding 4-year lag correlation during the former period is insignificant (r = −0.06). Note that, the variability period of WSC in the central North Pacific (near the dateline) is changed after late-1980s; the decadal variability is obvious after late-1980s, while the interannual variability is pronounced before late-1980s (Figure 23b).
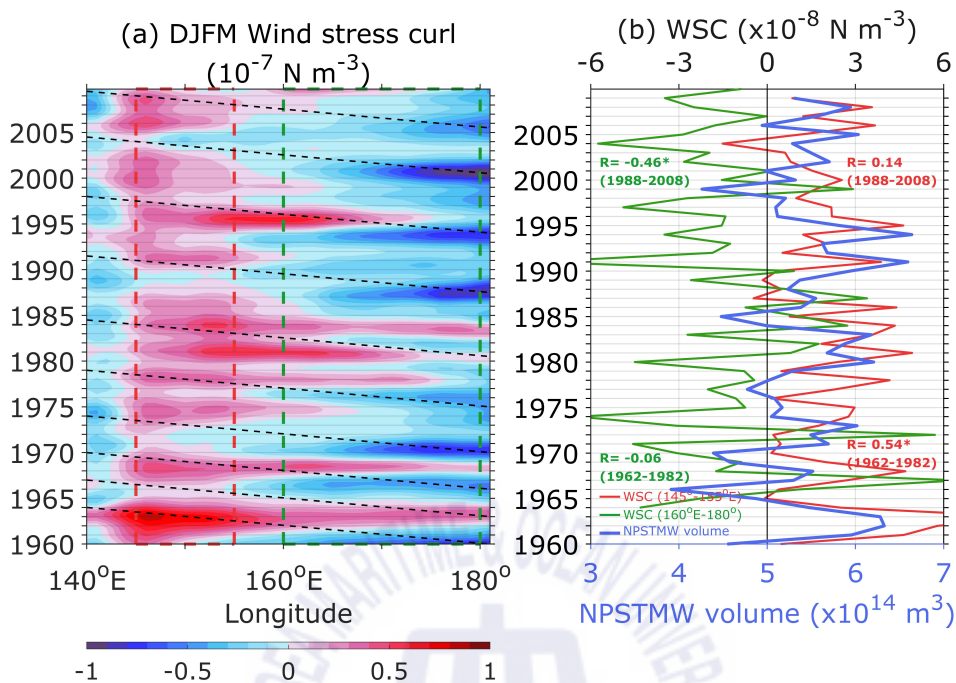
Figure 23. (a) The time-longitude Hovmöller diagram of the 3-year low-pass filtered DJFM wind stress curl, which is meridionally averaged between 33°N and 37°N. (b) Comparison between the NPSTMW volume in March (blue line) and the wind stress curl averaged in the NPSTMW formation region (145−155°E, 33−37°N, red line) and central North Pacific region (160°E−180°, 33−37°N, green line). The time axis of central North Pacific region (green line) is shifted +4 years to highlight the lagged relationship with the NPSTMW volume in March (blue line). Asterisk mark indicates statistically significant at the 90% confidence level.

Zonal and meridional wind stress patterns in the North Pacific are known to be influenced by the AL variability (Ishi & Hanawa, 2005; Kwon et al., 2010; Linkin & Nigam, 2008; Sugimoto & Hanawa, 2009). Sugimoto and Hanawa (2009) showed that the longitudinal (latitudinal) shift of the AL center is related to the PNA (WP) teleconnection pattern. To investigate the cause of the change in the WSC, the longitudinal and latitudinal position of the AL center is examined. The

central position of the AL is defined as a location of DJF SLP minimum in the region of 150°E−150°W, 30−60°N following Sugimoto & Hanawa (2009).

The latitudinal position of the AL center shows an obvious interannual-to-decadal variability during the total analysis period (Figure 24a). The dominant variability period is changed after late-1980s from interannual to decadal timescales. It is intriguing that the change of variability period is similar to the change of WSC variability in the central Pacific shown in Figure 23b (green line). The latitudinal position of AL center is significantly correlated with the WSC in the central Pacific (r = −0.56) (Figure 25). Because the center of action of WSC variability related with the meridional movement of the AL is situated at the central North Pacific (35°N, 175°W, Ishi & Hanawa, 2005), the meridional movement of the AL can affect the WSC variability and thus its zonal distribution. On the other hands, the longitudinal position of AL has an interdecadal variability with period of about 20 years (Figure 24b). For example, the central position of AL is located in the west (east) of dateline in 1970s and early 1990s (1980s and 2000s).

To figure out climate variability related with the AL postion change, DJF SLP is regressed on the time series of the AL's latitudinal and longitudinal position (Figure 26). The regression map on the AL latitudinal variation resembles the so-called NPO pattern, which is a north-south dipole structure of the SLP in the North Pacific (Figure 26a). In fact, the time series of the AL latitudinal variation is highly correlated with the NPO index (r = 0.62). On the other hands, the AL longitudinal variation is related with the first loading vectors of the SLP (AL mode) with a single SLP cell in the North Pacific (Figure 26b). The correlation coefficient between the SLP EOF PC-1 and the time series of the AL longitudinal variation is 0.61 and statistically significant at the 95% confidence level. These results are consistent with the previous study of Sugimoto and Hanawa (2009), who showed that the longitudinal and latitudinal shift of the AL is related to the PNA and WP teleconnection patterns, respectively.
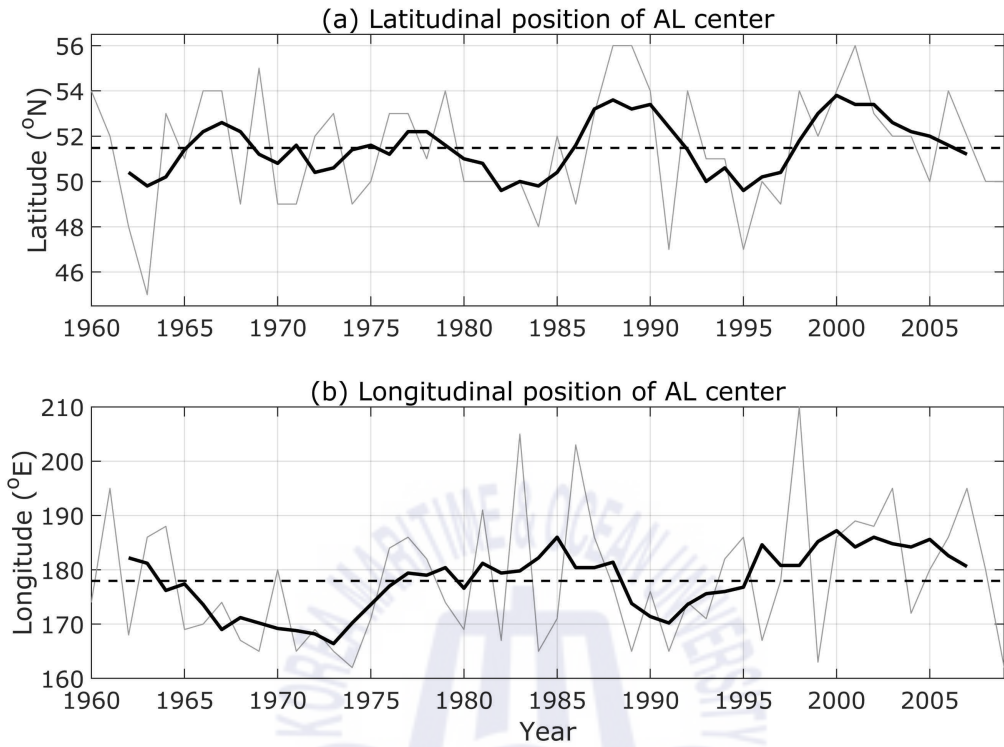
Figure 24. Time series of (a) latitudinal and (b) longitudinal position of the AL center. Thick lines indicate 5-year moving average values.
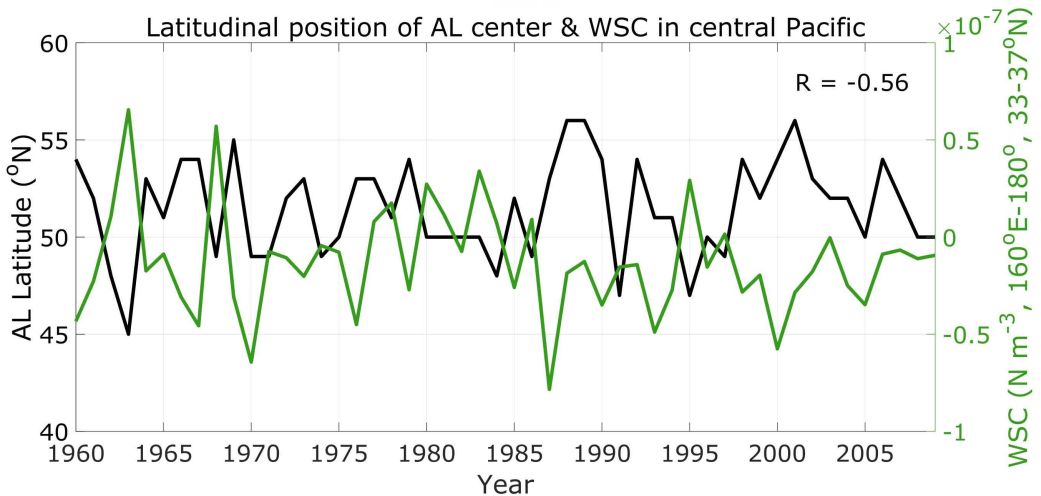
Figure 25. Time series of latitudinal position of the AL center (black) and the wind stress curl averaged in the central North Pacific region (160°E−180°, 33−37°N, green, same as green line in Figure 23b).
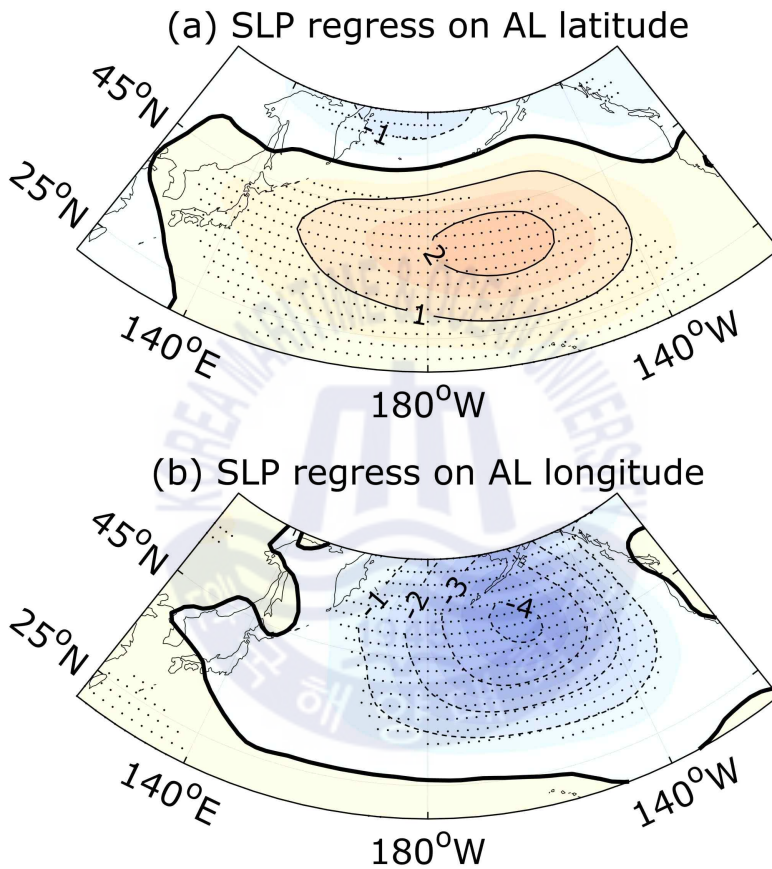
Figure 26. Regression maps of anomalous winter (DJF) SLP on (a) the latitudinal and (b) the longitudinal position of AL. Black dots indicate regions where the regression coefficients are statistically significant at the 95% confidence level.

The surface wind anomalies induced by the change of the AL position can modify the oceanic circulation in the North Pacific. To examine the response of the

oceanic circulation to the surface WSC change, the Sverdurp transport stream function was calculated in four different periods of AL variability; i.e., north/south AL and strong/weak AL (Sverdrup, 1947). North/south (strong/weak) AL periods are composed by exceeding plus/minus one standard deviation from the time series of the AL latitudinal (longitudinal) position. During the north (south) AL period, the boundary between the subtropical and subpolar gyre (i.e., zero-contour line) is shifted to the north (south) of 40°N (Figure 27a, 27b and 27c). The meridional shift of the subtropical/subpolar boundary is related with the north-south shifting of the zero WSC line. It can explain why the change of WSC variability in the central North Pacific is correlated with the meridional movement of the AL position (Figure 25). On the other hands, during the strong (weak) AL period, the strength of the subtropical and supolar gyre is enhanced (weakened) (Figure 27d, 27e and 27f). The change of WSC variability in the central North Pacific shown in Figure 23 and Figure 25 can be connected with the meridional movement of the AL position.
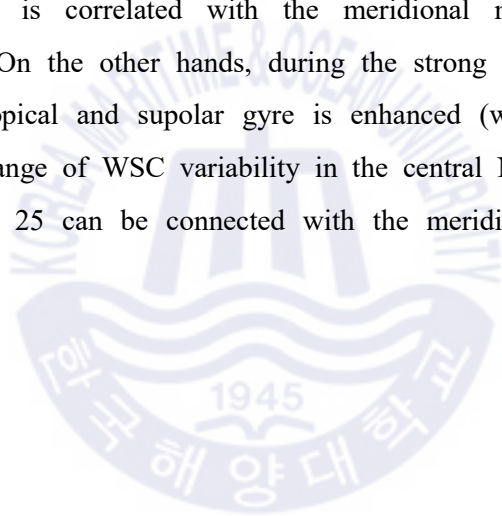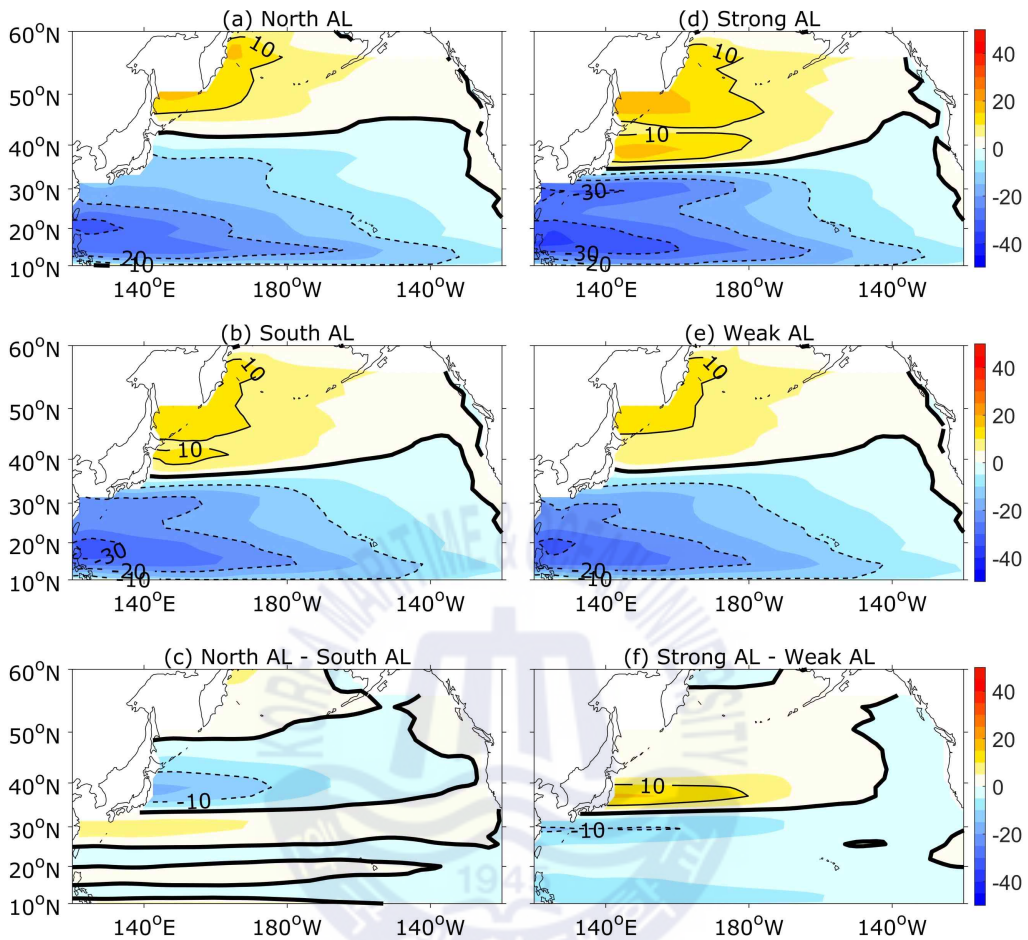
Figure 27. Composite maps of DJF Sverdrup stream function (Sv, 1 Sv = 10^6 m^3 s^{-1}). (a) North AL, (b) south AL, (c) difference between the north and south AL, (d) strong AL, (e) weak AL, and (f) difference between the strong and weak AL. Thick black lines indicate zero contour lines.

The WSC anomalies driven by the meridional shift of the AL can induce the change of SSH and isopycnal thickness in the pycnocline via Ekman pumping/suction. The baroclinic oceanic response to the WSC forcing can be estimated using a simple 1.5-layer reduced gravity model. Under the long-wave approximation, the linear vorticity equation is

$$\frac{\partial h}{\partial t} - C_R \frac{\partial h}{\partial x} = - \frac{g'}{\rho_0 g f} \boldsymbol{K} \bullet \ \nabla \times \tau, \tag{11}$$

where h is the SSH, C_R is the speed of the long baroclinic Rossby wave, f is the Coriolis parameter, ρ_0 is the reference density of seawater, g' is the reduced gravity (0.027 m s^{-2}), $\boldsymbol{K}$ is the unit vector in the vertical direction, and $\nabla \times \tau$ is the WSC. Integrating equation (11) from the eastern boundary (x_e) along the baroclinic Rossby wave characteristics, equation (12) can be obtained as (Fu & Qiu, 2002; Qiu, 2003)

$$h(x,t) = \frac{g'}{\rho_0 g f C_R} \times \int_{x_e}^{x} \boldsymbol{K} \bullet \ \nabla \times \tau(x', t + \frac{x - x'}{C_R}) dx'. \tag{12}$$

The eastern boundary condition is assumed to be $h(x_e, t) = 0$. Following Qiu (2003), the phase speed of the long baroclinic Rossby wave is set to 0.023 m s^{-1} at 38°N, and 0.041 m s^{-1} at 32°N, because the Rossby wave speed varies with latitude.

To examine how the ocean surface response to the position shift of AL, the SSH is estimated by equation (12) using the regressed WSC on the latitudinal position of the AL center. Figure 28 shows the Hovmöller diagram of the hindcast SSH anomaly meridionally averaged between 32°N and 38°N, which corresponds to the main formation area of the NPSTMW. It is notable that positive/negative anomalies of SSH propagate westward from the central Pacific after late-1980s. It is intriguing that the SSH anomalies change in decadal time scales: positive (negative) anomalies in late-1980s and late-1990s (early-1990s and mid-2000s). This result is also consistent with the decadal variability of the 25.7 kg m^{-3} and WSC in the central Pacific after late-1980s (Figure 21 and Figure 23). On the other hands, before late-1980s, the westward propagating signals are not so much clear, especially in 1970s and early-1980s, which correspond to small fluctuations of the AL latitude before late-1980s (Figure 24a).
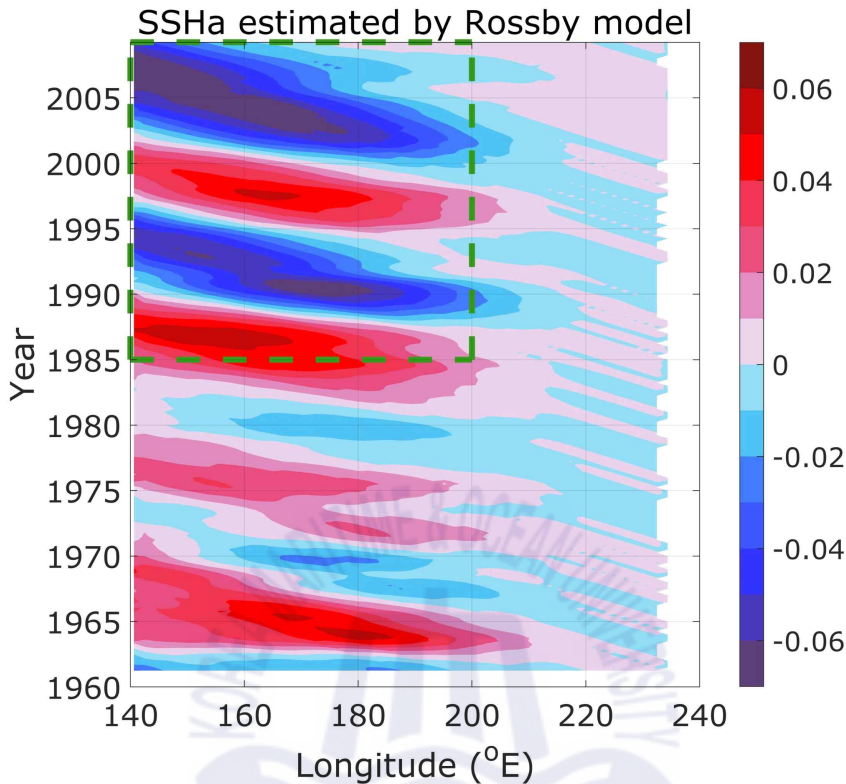
Figure 28. The time-longitude Hovmöller diagram of the estimated SSH anomaly (m), which is meridionally averaged between 32°N and 38°N.

Figure 29 shows the regressed SLP on the NPO index of each period. During 1962−1982, the dipole centers are located on 157°W with strong north-south SLP gradient. It appears that the center moves eastward by 10° and the SLP gradient is decreased at the same time during 1988−2008. Yeh et al. (2018) suggested that the center of NPO is shifted from the western Pacific to the eastern Pacific after mid-1990s compared to before the mid-1990s. Pak et al. (2014) also showed that the EAWM and NPO were significantly correlated to each other during the 1973−1987 strong winter monsoon epoch, but their correlation practically vanishes during the 1988−2002. They also reported that the EAWM's impact on SST during the

latter epoch shrank remarkably into a limited area in the East China Sea, making a clear distinction from the NPO impact. Therefore, it is supposed that the eastward shift of the NPO and weakening of the EAWM cause the change the effect of the local atmospheric forcing. When the NPO centers are placed closer to the KE region before the late-1980s, the direct local atmospheric forcing associated with the NPO dominantly influences the formation of the NPSTMW and suppresses the effect of the remote forcing, while the former weakens and is replaced by the latter when the NPO moved eastward after the late-1980s. This can be one of reasons why the lag of correlation between the NPO and the NPSTMW volume is changed before and after late-1980s (Figure 20b and Figure 20c).
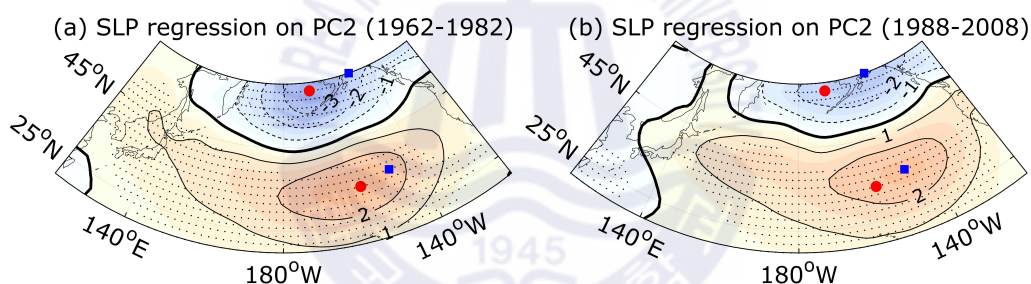
Figure 29. Regression maps of anomalous winter (DJF) sea level pressure on the NPO index for the period of (a) 1962−1982 and (b) 1988−2008. Red dots and blue squares represent the two centers of action of NPO during 1962−1982 and 1988−2008, respectively. Black dots indicate regions where the regression coefficients are statistically significant at the 90% confidence level.

The variability of the surface heat flux is examined to check the linkage between the late-1980s regime shift of the NPSTMW formation and the change of the local air-sea interaction. Figure 30 shows the domain averaged DJFM surface heat flux in the study area (135−164°E and 30−42°N) and its 21-years moving standard

deviation. The surface heat flux shows an obvious interannual variation before late-1980s (Figure 30a). The variability of the surface heat flux gradually decreases from 1960s to 2000s (Figure 30b), which is consistent with the change of the ASI variability (Figure 16b). Strong (weak) variability of the surface heat flux during 1962−1982 (1988−2008) should be related with the EAWM as suggested by Park et al. (2012) and Pak et al. (2014, 2019), who showed that the contribution of the EAWM to the air-sea interaction in the KE region has significantly changed around 1990. Therefore, it should be noted that the direct local atmospheric forcing associated with the EAWM also influences the late-1980s regime shift of the NPSTMW formation, although, the linkage between the EAWM and the change of the AL position is not investigated in this study.
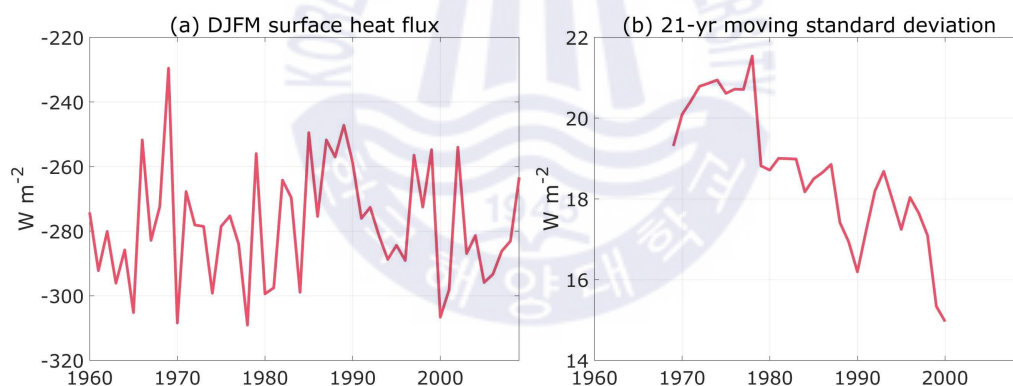
Figure 30. (a) Time series of DJFM surface heat flux averaged over the analysis area (135−164°E and 30−42°N). (b) 21-year moving standard deviation of the DJFM surface heat flux.

Chapter 4. NPSTMW formation in Kiel Climate Model

4.1 Model validation

To check the KCM performance, the simulated MLD is compared with the Holte et al. (2017)'s MLD data derived from the Argo floats during 2000−2013. The simulated NPSTMW thickness is also compared to that estimated from the Argo floats and sea surface height during 2001−2011 provided by Kuroshio Extension System Study (Rainville et al., 2014). The simulated SLP is validated with the CORE2-IAF dataset during 1960−2009 (Large & Yeager, 2009). The EN4 dataset (Good et al., 2013) is also used to evaluate the simulated low-PV structure of the NPSTMW.

The KCM reproduces deep MLD region (>150 m) along the KE, which is consistent with the observation (Figure 31). However, the deep MLD region in the KCM is merged into a single MLD pool probably due to the coarse horizontal resolution (~0.5°), which is different from the observed MLD, which has two maxima in 30−35°N, 35−42°N region. The NPSTMW is generally located south of the Kuroshio in the latitude band from 20°N to 35°N. The KCM well reproduces the spatial distribution of the NPSTMW thickness compared to that of the observation (dashed lines), although there is an overshooting of the Kuroshio (green lines). In this study, thick NPSTMW region (>100 m) is considered as the main formation area of the NPSTMW and a study region (140−180°E and 20−35°N; box in Figures 31b).
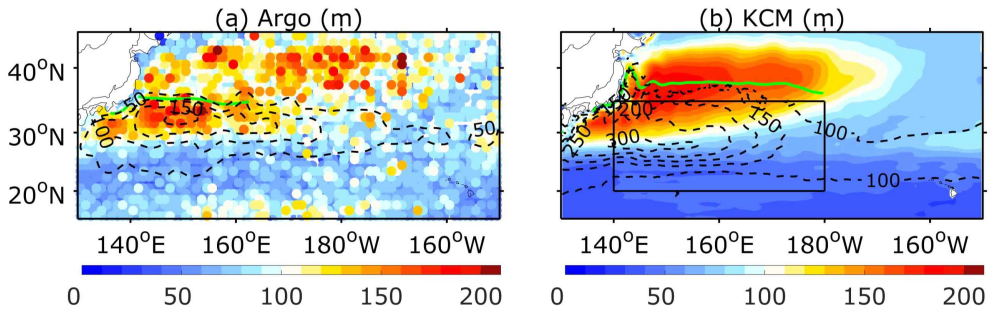
Figure 31. Mixed layer depth (m, color shaded) from (a) the Argo observation (2000−2013, Holte et al., 2017) and (b) the KCM during the cooling seasons (December to following March). The MLD is defined by the criterion with the density difference from the depth of 10m as $\Delta\sigma_\theta = 0.03$ kg m^{-3}. Dashed lines denote the NPSTMW thickness (m) from (a) the Argo floats and sea surface height during 2001−2011 provided by Kuroshio Extension System Study (Rainville et al., 2014) and (b) the KCM. Green lines indicate the Kuroshio main axis defined as the 12°C isotherm at the depth of 300 m from (a) the World Ocean Atlas 2009 and (b) the KCM. Box in (b) indicates the study region in this study.

To validate the simulated NPSTMW in the formation area, the vertical section of the PV along the 145°E is compared between the KCM and EN4 (Figure 32). Compared with the EN4, the KCM reproduces well the vertical distribution of the low-PV water (PV $< 2.0 \times 10^{-10}$ m^{-1} s^{-1}), which is located at the subsurface layer between 100 and 300 m in the latitude band from 20°N to 35°N. The density range of the simulated low PV water is relatively lighter ($24.6 < \sigma_\theta < 25.2$ kg m^{-3}) than the observation ($25.0 < \sigma_\theta < 25.5$ kg m^{-3}). For example, the simulated PV minimum appears in the density range between 24.8 and 25.0 kg m^{-3} (Figure 32b), while the observed one appears relatively denser density range (25.2−25.4 kg m^{-3}) (Figure 32a). The difference of the NPSTMW density range between the model and observation may be associated with surface heat flux biases and overshooting of the Kuroshio (Xu et al., 2014). In this study, the NPSTMW is

- 50 -

defined by a potential density anomaly (σ_θ) range of 24.6−25.2 kg m^{-3} and the low PV ($<2.0 \times 10^{-10}$ m^{-1} s^{-1}) conditions. The minimum thickness of the NPSTMW was set to 50 m as suggested by Douglass et al. (2012).
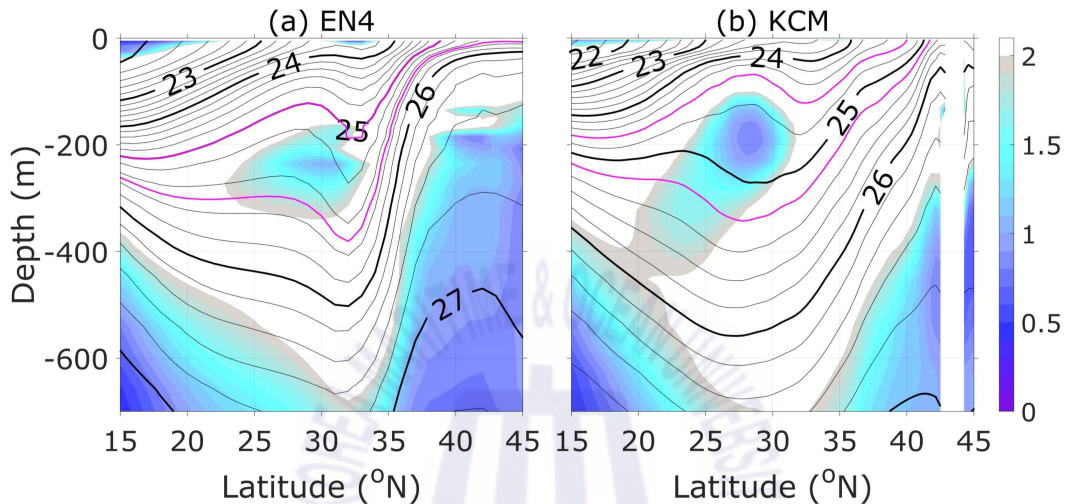
Figure 32. Meridional sections at 145°E of climatological mean PV (10^{-10} m^{-1} s^{-1}, color shaded) for (a) the observation (EN4, 1960−2014) and (b) the KCM. Black solid lines indicate the mean potential density (kg m^{-3}). The contour interval for the potential density is 0.2 kg m^{-3}. Magenta lines indicate the isopycnal layers of $\sigma_\theta = 25.0$, 25.5 kg m^{-3} for the observation and $\sigma_\theta = 24.6$, 25.2 kg m^{-3} for the KCM.

The horizontal distribution of the simulated winter SLP is also compared to the observation (Figure 33). The KCM reproduces the feature of the winter SLP distribution, especially the location of the SLP minimum (cross marks), although the minimum pressure in the KCM (1,003 hPa) is somewhat higher than that in the observation (1,000 hPa). The difference in the minimum pressure between the KCM and observation may be associated with the different CO_2 conditions. It is reported that the central pressure of the AL has been deepened since the 20th century (Deser & Phillips, 2009; Gillett et al., 2003; Lu et al., 2004). In addition,

the two leading EOFs of the DJFM mean SLP anomaly is calculated to validate the winter SLP variability in the North Pacific region (120°E−120°W, 20−60°N). The KCM reproduces well the AL pressure pattern (Trenberth & Hurrell, 1994) and the NPO pattern (Linkin & Nigam, 2008) as for the first and second loading vectors of the SLP, respectively (Figure 34). This result is consistent with that of the CORE2-IAF (Figure 19).
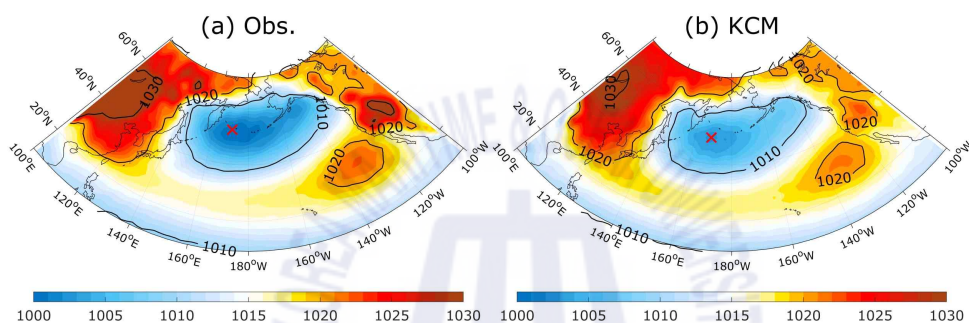
Figure 33. Climatological mean sea level pressure (hPa) for (a) the observation (NCEP, 1960−2009) and (b) the KCM during the cooling seasons (December to following March). Red cross marks denote the locations of the SLP minimum.
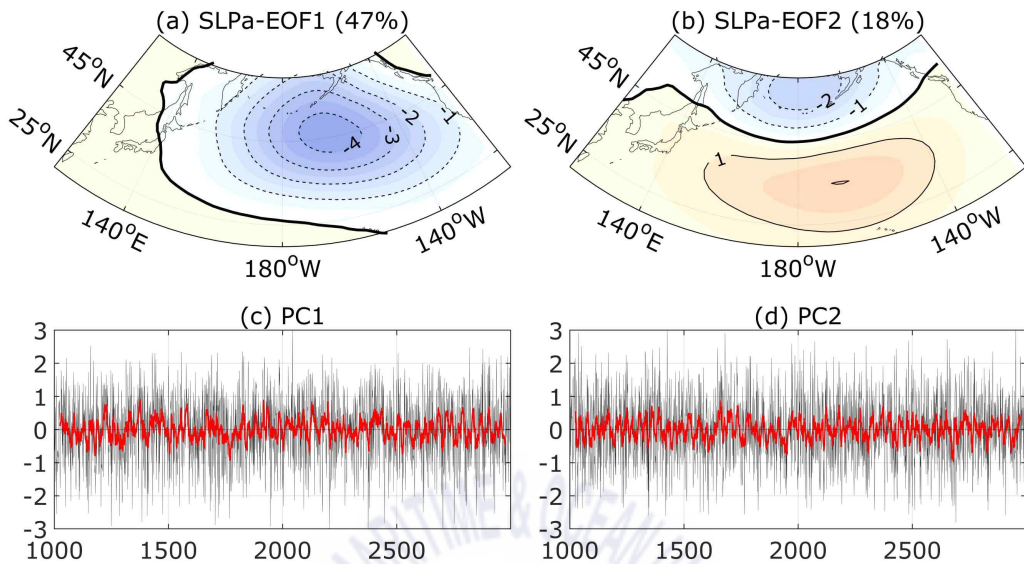
Figure 34. (a) First and (b) second EOFs of the DJFM mean sea level pressure anomaly over the North Pacific region (120°E−120°W, 20−60°N). (c-d) PC time series for the (c) first and (d) second EOFs of the SLP anomaly. Thick red lines indicate the 10-year moving averaged PC time series.

Figure 35 shows the time series of the AL center position. The central position of the AL is defined as a location of the DJF SLP minimum over the region of 150°E−150°W, 30−60°N. The time mean position of the AL center is located at 177.3°E, 49.6°N, which is similar compared to that of observed one (178.4°E, 51.6°N) from the CORE2-IAF. There is remarkable interannual-to-decadal variability in both latitudinal and longitudinal positions of the AL center. To examine the variability of both time series, a power spectra analysis is performed (Figure 38). The most dominant peak in the latitudinal position is found at decadal time scales with maximum power at periods of about 10 years, while the longitudinal position of AL has a peak at slightly longer periods (15 years). This result is consistent with the previous result (Figure 24) in Section 3.4 and that of based on the

observation data by Sugimoto and Hanawa (2009), who showed that the longitudinal (latitudinal) variation of the AL center has an interdecadal (decadal) timescales about 20 years (10 years). The interannual variability (less than 10 years) is also significant in both time series.

To check the persistency of variability of the AL position, a wavelet analysis is conducted after filtered by 5-year moving average from each time series (Figure 37). Both longitudinal and latitudinal positions of the AL center have a significant power in the periodicity band of 8−32 years. Although a significant power is observed within the band of 32−256 in both wavelet power spectra, those low-frequency signals are not persistent during the total analysis period. Therefore, the decadal signals will be focused on this study, because the variability of the AL central position may be related with the regime shift of the NPSTMW formation as shown in Section 3.4.

To figure out which climate variability is related with the central position of AL, DJF SLP is regressed on the latitudinal and longitudinal position of AL center (Figure 38). The regression map of AL latitude resemble the NPO pattern with a north-south dipole SLP pattern (Figure 38a). The meridional variation of the AL position is significantly correlated with the NPO index ($r = 0.64$). On the other hands, the zonal variaion of the AL position is related with the first loading vectors of the SLP with a single SLP cell (Figure 38b). The correlation coefficient between the SLP EOF PC-1 and the longitudinal position of the AL center is significant ($r = 0.54$). These results are consistent with the results in Section 3.4 and the previous study of Sugimoto and Hanawa (2009).
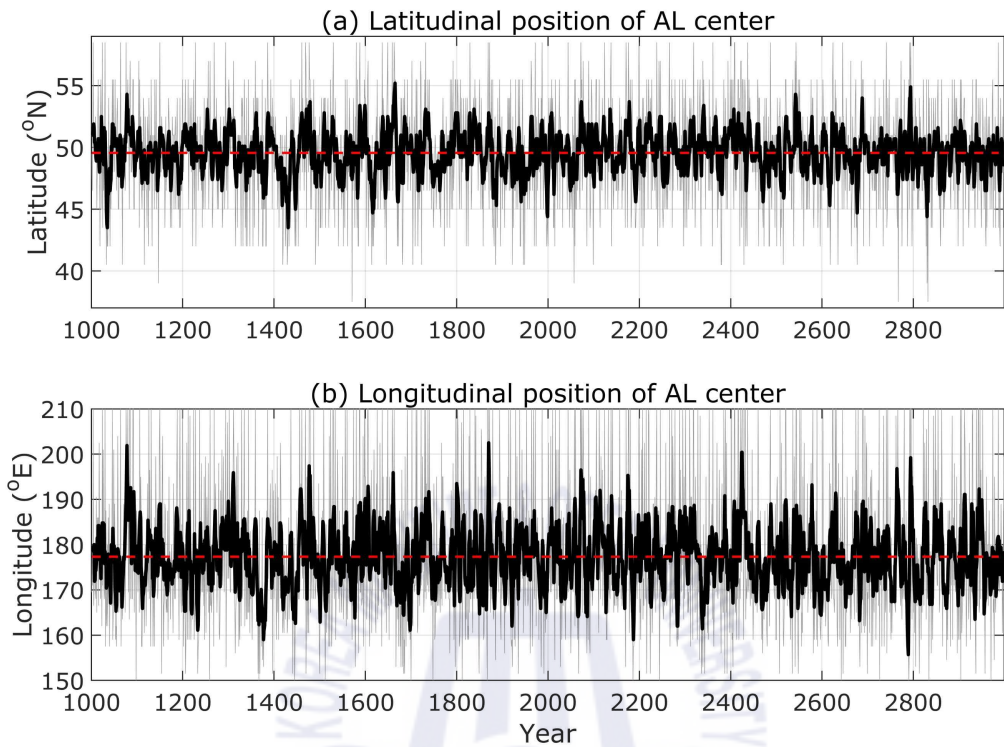
Figure 35. Time series of (a) latitudinal and (b) longitudinal position of the AL center. Thick solid lines indicate 5-year moving average values. Red dashed lines denote the time mean values.
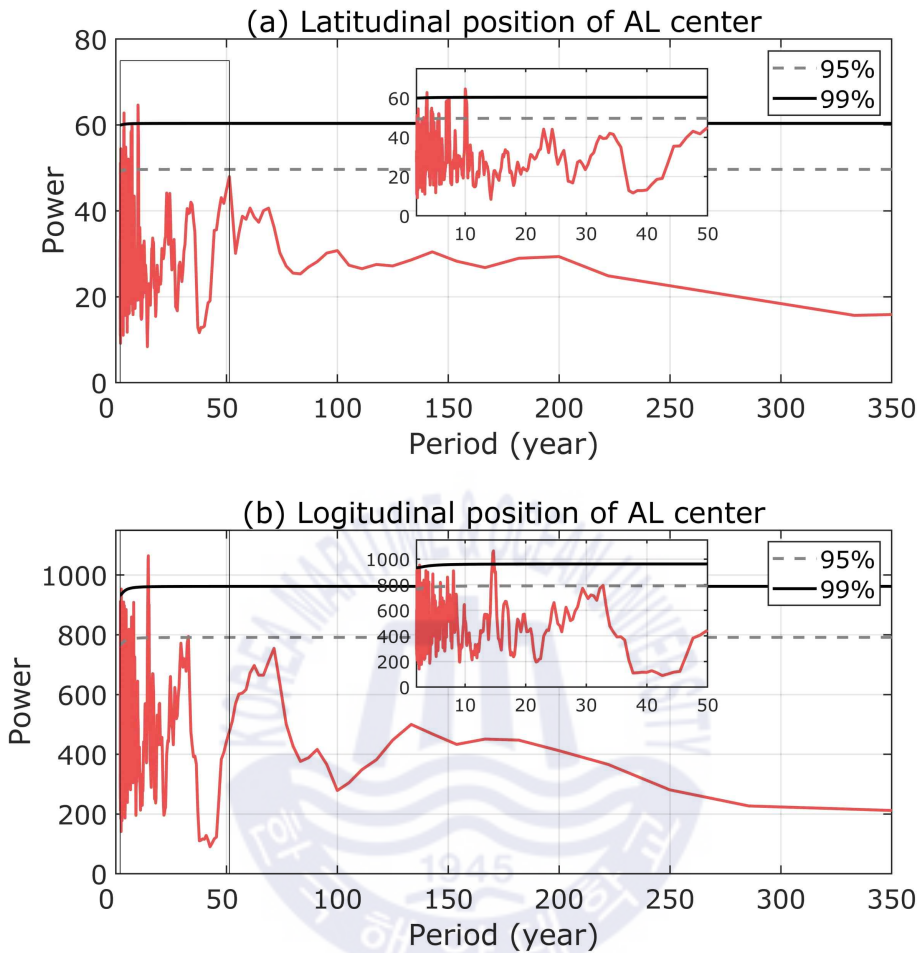
Figure 36. Power spectrum of (a) the latitudinal and (b) longitudinal position of the AL center. Solid and dashed lines denote the 99% and 95% confidence spectrum, respectively.
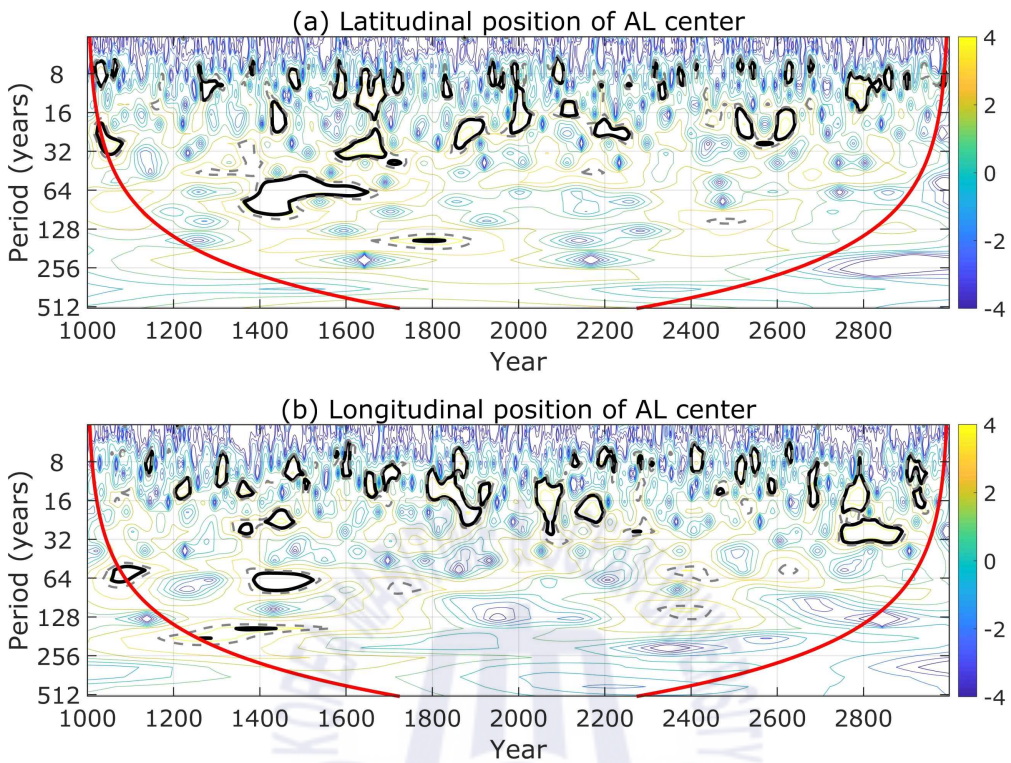
Figure 37. Wavelet power spectrum for (a) latitudinal and (b) longitudinal position of the AL center. Solid black and dashed-gray contours denote the regions where the confidence level exceeds 95% and 90%, respectively. Red line indicates the "cone of influence".
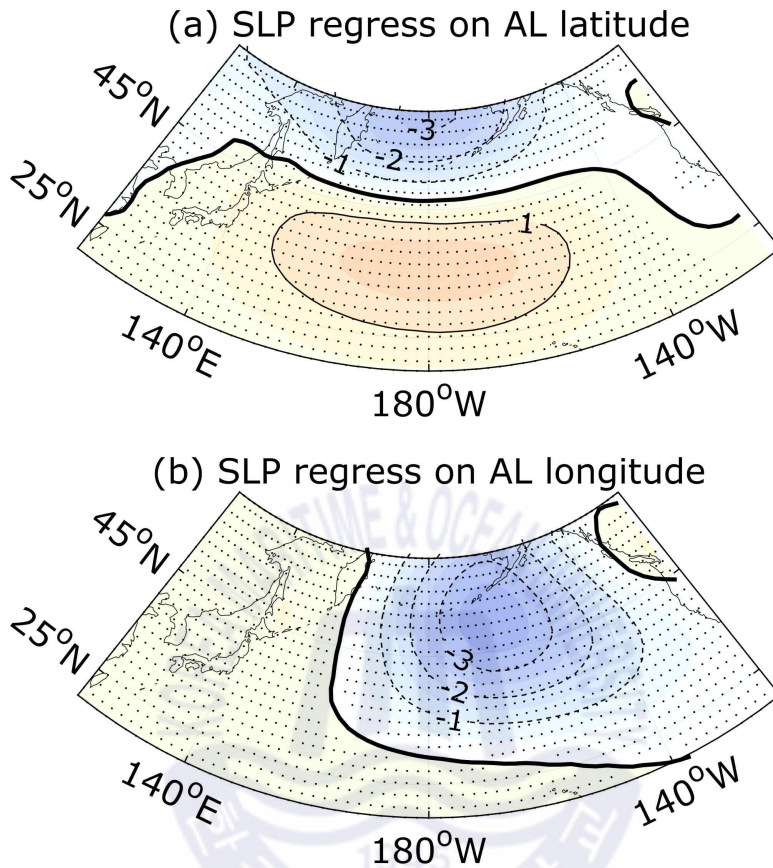
Figure 38. Regression maps of anomalous winter (DJF) SLP on (a) the latitudinal and (b) the longitudinal position of AL. Black dots indicate regions where the regression coefficients are statistically significant at the 95% confidence level.

To examine the response of the oceanic circulation to the surface WSC change, the Sverdurp transport stream function is calculated in four different periods of AL variability; i.e., north/south AL and strong/weak AL (Figure 39). North/south (strong/weak) AL periods are composited by exceeding plus/minus one standard deviation from the time series of the AL latitudinal (longitudinal) position. During the north (south) AL period, the boundary between the subtropical and subpolar

gyre (i.e., zero-contour line) is shifted to the north (south) of 40°N. The meridional shift of the subtropical/subpolar boundary is related with the north-south shifting of the zero WSC line. On the other hands, during the strong (weak) AL period, the strength of the subtropical and subpolar gyre is enhanced (weakened).

In Section 3.4, the movement range of AL latitude is much wider during ENT epoch (about 10°) than that of during ASI epoch (about 6°) (Figure 24a). To investigate the relationship between the meridional movement of the AL center and the regime shift in the NPSTMW formation, the latitudinal position of the AL center is composited in both ASI and ENT epoch (Figure 40). The median values of the AL center is almost same (about 49.5°N) in both epochs. During the ASI epoch, the north-south movement range of the AL center is by about 3° ranging from 48°N to 51°N. On the other hands, during the ENT epoch, the center of AL is located further south at around 46.5°N and thereby the north-south movement of the AL center is much wider (about 4.5°; 46.5°N–51°N) than that of during ASI epoch. This result is consistent with the result shown in Section 3.4 (Figure 24a).
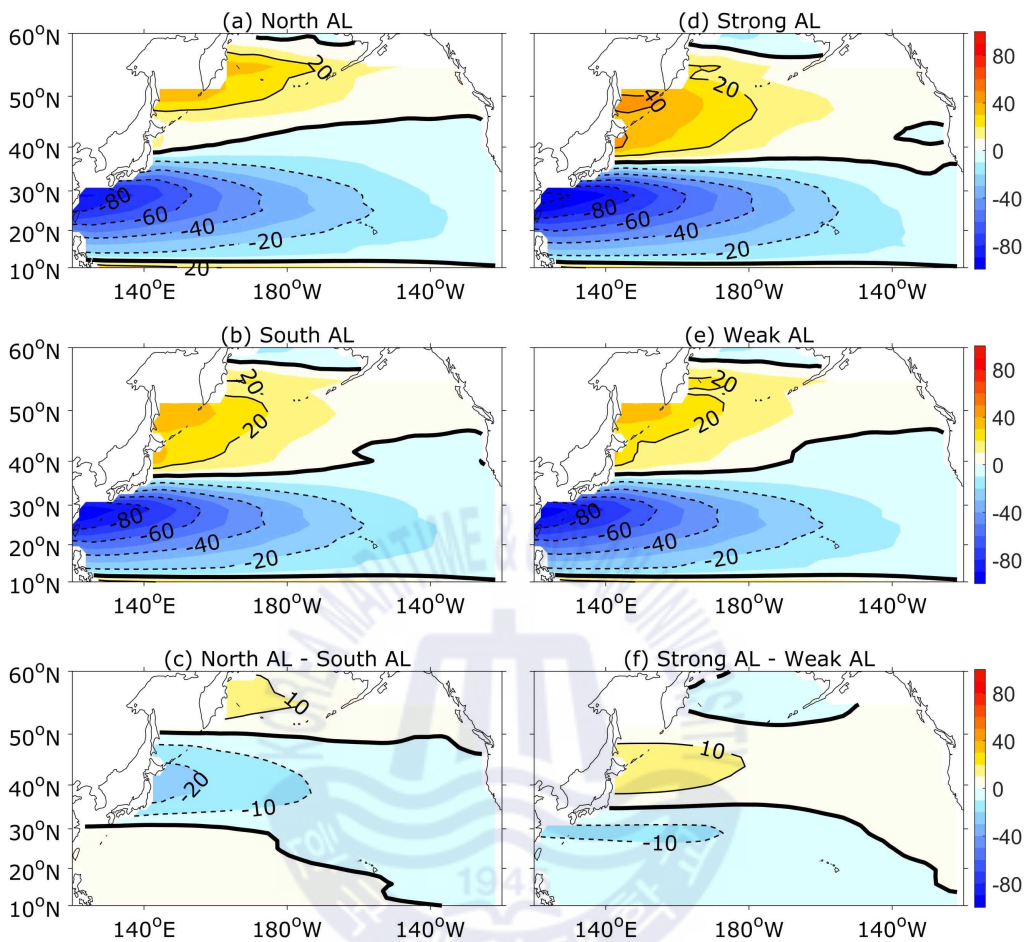
Figure 39. Composite maps of DJF Sverdrup transport stream function (Sv, 1 Sv = 10^6 m^3 s^{-1}). (a) North AL, (b) south AL, (c) difference between the north and south AL, (d) strong AL, (e) weak AL, and (f) difference between the strong and weak AL. Thick black lines indicate zero contour lines.
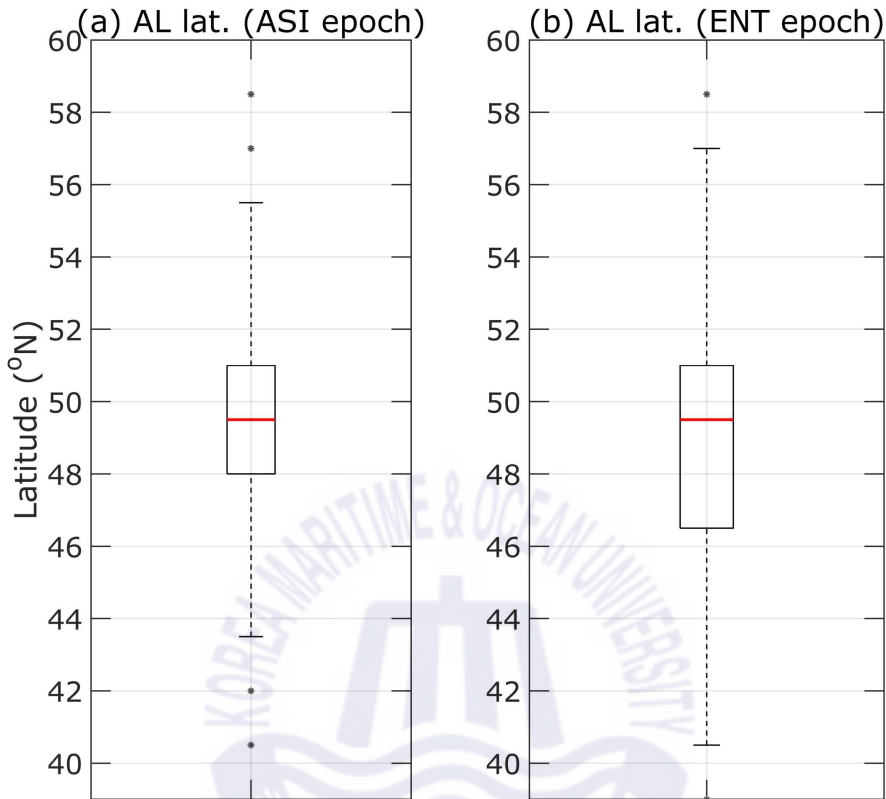
Figure 40. Box-and-whisker plot for the latitude of AL center during (a) ASI epoch and (b) ENT epoch. The solid boxes indicate 25th and 75th percentiles, and the thick red lines in the box is the median value of the AL latitude. The whiskers (upper and lower dashed lines) correspond to the 0.7^{th} and 99.3^{th} percentiles of the samples. Asterisk marks (outliers) denote that the latitude beyond the whisker (0.7^{th} and 99.3^{th} percentiles).

4.2 Variability of the NPSTMW formation in Kiel Climate Model

To identify the key parameters affecting the NPSTMW formation during winter, the volume budget analysis is conducted by equation (9) in the formation area of the NPSTMW. The result show that two terms, ASI (1.83×10^{14} m^3) and ENT

- 61 -

(1.54×10^{14} m^3), dominate for the NPSTMW formation during winter, while ADV (0.04×10^{14} m^3) and residual (-0.52×10^{14} m^3) have relatively minor roles in the NPSTMW formation (Figure 41). The time mean values of the volume budget terms are similar to those in the OGCM described in Chapter 3 (Table 2) except for the ADV term. The difference in the ADV term between the KCM and the OGCM may be associated with the different density range of the NPSTMW (KCM: $24.6-25.2$ kg m^{-3} and OGCM: $25.1-25.7$ kg m^{-3}). It is noted that the ENT, which reflects primarily the ocean dynamics, has little correlation with the ASI term ($r = -0.13$) in the NPSTMW volume budget analysis. It is also noted that the NPSTMW volume in March (blue line in Figure 41) and DJFM integrated formation ($\partial V/\partial t$) term (black line in Figure 41) show a similar temporal evolution ($r = 0.54$), although the volume budget terms are calculated without imposing the low PV constraint. Therefore, the NPSTMW volume in March is used to compare with the other budget terms (ASI and ENT terms).

The most obvious feature in each time series is the apparent interannual-to-decadal variability (Figure 41). To identify the dominant time scales of variability, a power spectra analysis is conducted (Figure 42). The NPSTMW volume in March shows a statistically significant variability at the period less than 10 years (Figure 42a). The ASI and ENT also have clear interannual and sub-decadal variations with a periodicity less than 10 years (Figure 42b and Figure 42c). The most dominant peaks is located at 8 years in both ASI and ENT terms.
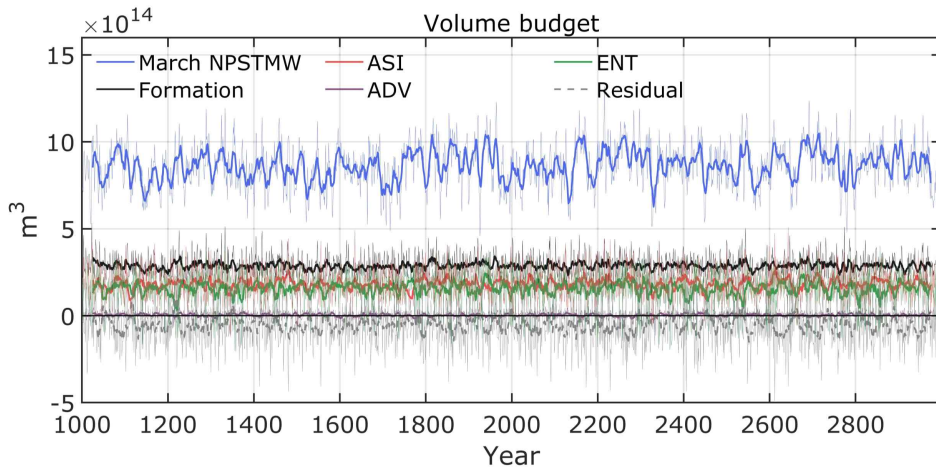
Figure 41. Time series of volume of the NPSTMW in March (blue) and volume budget terms of equation (2). Volume budget terms integrated during cooling seasons (DJFM) include volume formation (black), air-sea interaction (ASI, red), advection (ADV, purple), vertical entrainment (ENT, green), and residual (dashed gray) terms. Thick lines indicate the 10-year moving averaged each time series.

Table 2. Time-averaged values of the volume budget terms in the KCM and the OGCM.

Volume budget terms ($\times 10^{14}$ m^3)	KCM (1000−2999)	OGCM (1960−2009)
Formation	2.89	2.11
Air-sea interaction (ASI)	1.83	1.65
Vertical entrainment (ENT)	1.54	1.85
Advection (ADV)	0.04	−0.88
Residual	−0.52	−0.51
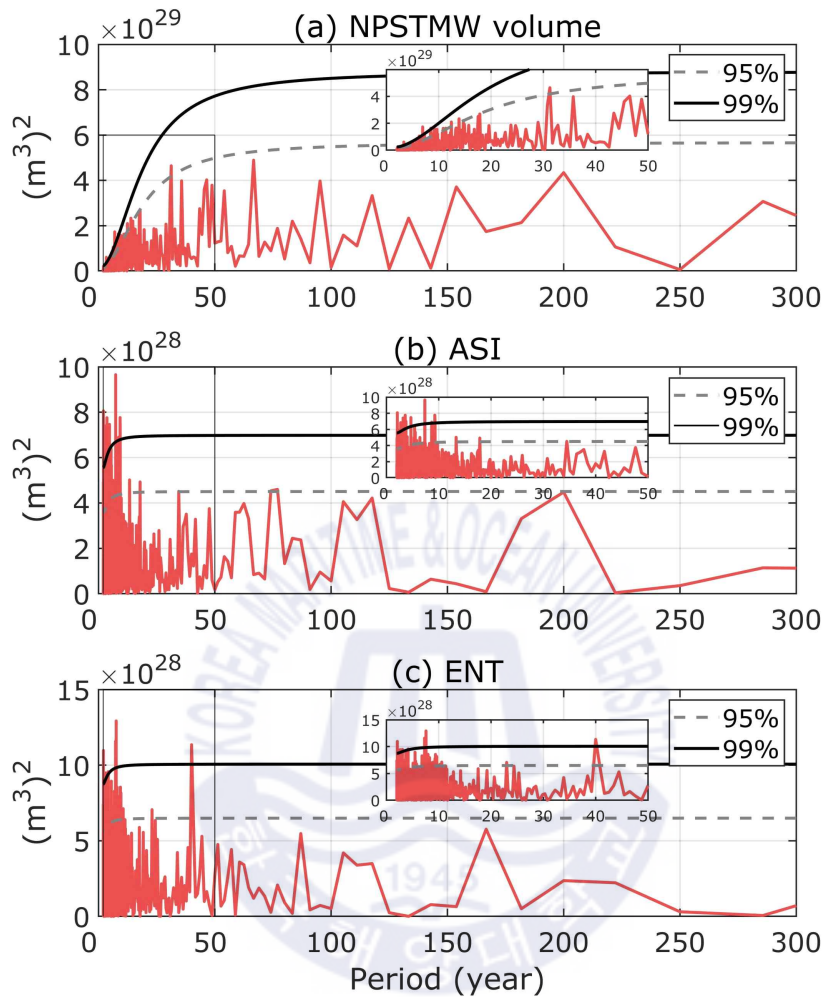
Figure 42. Power spectrum for (a) the NPSTMW volume in March, (b) ASI, and (c) ENT. Solid and dashed lines are the 99% and 95% confidence spectrum, respectively.

To examine the change of driving factors for the NPSTMW formation, the moving correlation coefficients is calculated between the NPSTMW volume and formation terms in equation (9) (Figure 43). The moving window size is set to 31-year by considering interannual-to-decadal variability of the NPSTMW volume, volume budget terms (Figures 42). The most striking feature in time evolution of

both moving correlation coefficients is the successive changes of the driving mechanism for the NPSTMW formation. For example, during 1130−1180, the ocean dynamics term is significantly correlated with the NPSTMW volume in March at 95% confidence level, while local ASI term has no significant correlation with it. In turn, during 1230−1280, the local ASI exhibits a significant correlation with the NPSTMW volume at 95% confidence level, but the ocean dynamics term does not. It is noted that both time series of moving correlation coefficients between the volume budget terms and the NPSTMW volume is significantly negatively correlated with each other ($r_{ASI\_NPSTMW \ \& \ ENT\_NPSTMW}$ = −0.28) at 95% confidence level. This result is consistent with the previous finding in Section 3.3, showed a sudden change of the driving mechanism for the NPSTMW formation in late-1980s using an OGCM simulation. The results are robust regardless of the moving window length between 21 and 61 years (Figure 44).

Considering the contrasts of the moving correlation coefficients in Figure 43, the total analysis period is separated into two distinct epochs, i.e., ASI epoch and ENT epoch, respectively. The following two criteria are applied to determine each epoch: (1) the correlation coefficient must be higher than the other one; and (2) correlation coefficient must be higher than 0.3, which corresponds to a marginal significance at 90% confidence level. 799 (~40% of total analysis period) and 562 (~28% of total analysis period) years are selected as the ASI and ENT epoch, respectively. In this study, the time series of the moving correlation coefficients between the volume budget terms and the NPSTMW volume (i.e., r_{ASI_NPSTMW} and r_{ENT_NPSTMW}) are used as the indices to represent the ASI and ENT epoch, respectively.

It is remarkable that the transitions of the driving factors for the NPSTMW formation periodically occurred in multi-decadal time scale. To examine the variability of each epoch, a power spectra analysis is performed on the indices of the ASI (r_{ASI_NPSTMW}) and ENT (r_{ENT_NPSTMW}) epoch (Figure 45). Both epoch indices

vary from multi-decadal to sub-centennial timescales. Statistically significant peaks are located at periods of about 70−90 years. The most dominant peak in both epochs is found at multi-decadal timescales with maximum power at periods of about 80 years. This result suggests that the driving factors for the NPSTMW formation is changed in multi-decadal timescales.

To quantitatively estimate how long the NPSTMW is affected by each forcing, the persistence time is calculated as the duration periods (between the start and finish year; denoted in Figure 43) of each ASI and ENT forcing. Figure 46 shows box-and-whisker plot of the persistence time for each forcing. Both ASI and ENT forcing persists during about 10−30 years. In the ASI (ENT) forcing, the upper and lower bounds of the box (25th and 75th percentiles) are located between 7 and 24 years (9 and 32 years) and the median value is 13 years (20 years). It is noted that the persistence time of 10−30 years is similar to the findings of Pak et al. (2019), who showed that the driving mechanisms of the winter SST variability in the KE region is changed in early 1990s (from the refreshening to reemergence mechanism) and mid-2000s (from the reemergence to refreshening mechanism). To sum up, the driving factors for the NPSTMW formation is changed in multi-decadal time scales. Once the epoch changes, each forcing persists during about 10−30 years.
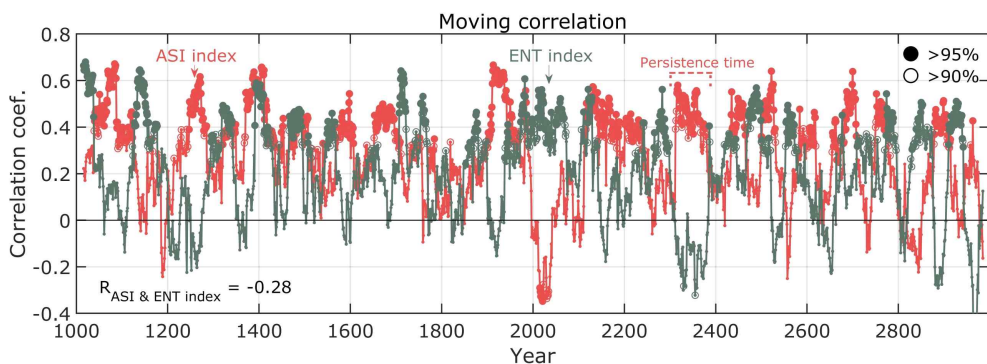
Figure 43. The 31-year moving correlation coefficient of the NPSTMW volume in March with the air-sea interaction (red) and the ocean dynamics (vertical entrainment, cobalt green) terms. Closed and open circles indicate significant correlation coefficients at the 95% and 90% confidence level, respectively. The 31-year moving correlation is the correlation between two time series within the window of ±15 years relative to the corresponding year.
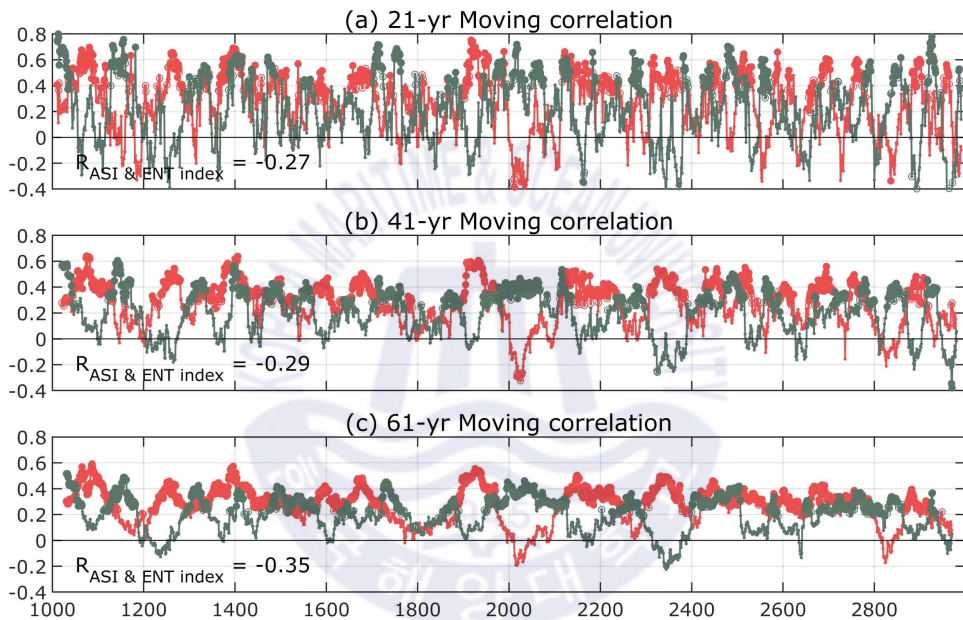
Figure 44. (a) The 21-year moving correlation coefficient of the NPSTMW volume in March with the air-sea interaction (red) and the ocean dynamics (vertical entrainment, cobalt green) terms. Closed and open circles indicate significant correlation coefficients at the 95% and 90% confidence level, respectively. The 21-year moving correlation is the correlation between two time series within the window of ±10 years relative to the corresponding year. (b,c) Same as in (a), but for (b) the 41-year and (c) 61-year moving correlation coefficient.
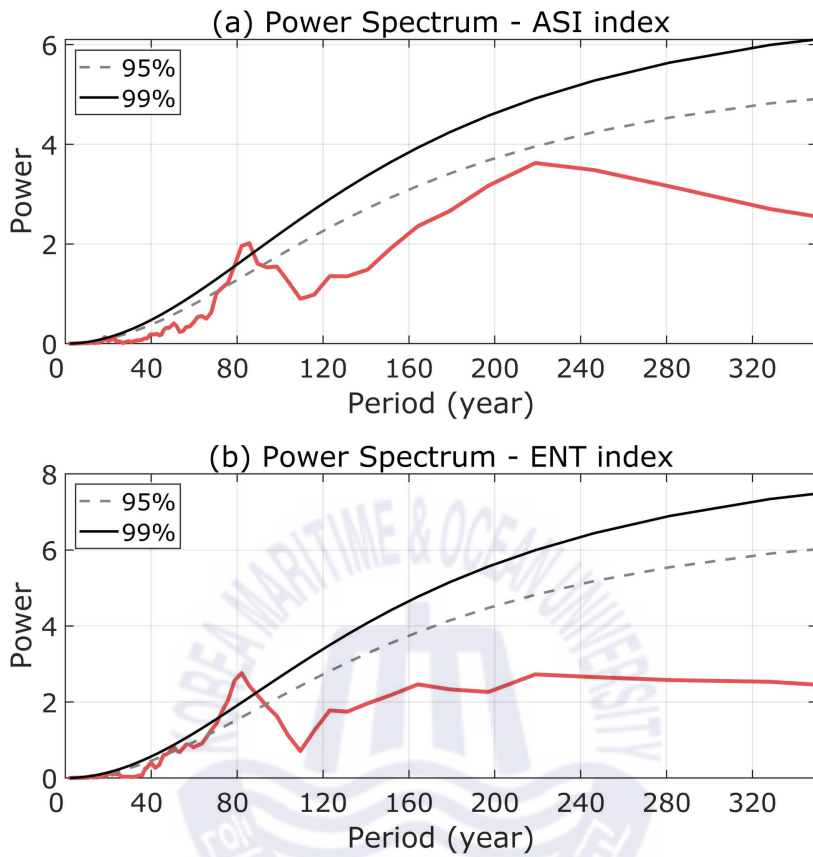
Figure 45. Power spectrum of (a) the ASI index and (b) ENT index. Solid and dashed black lines are the 99% and 95% confidence spectrum, respectively.
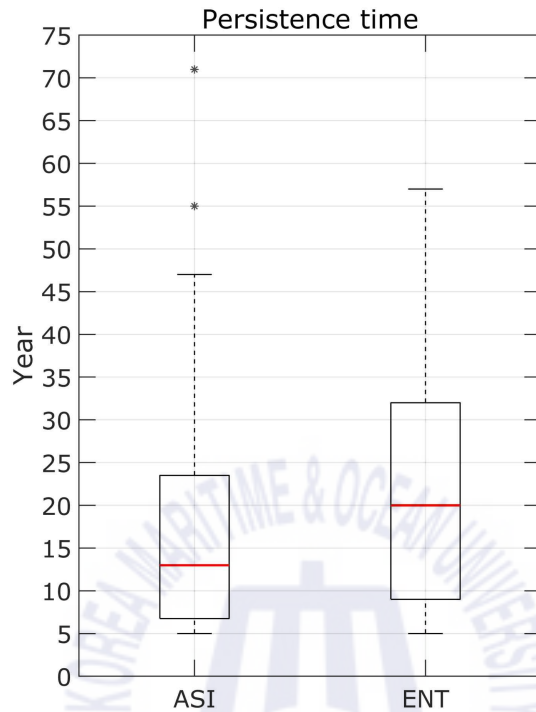
Figure 46. Box-and-whisker plot for the persistence time, which is calculated as the duration periods (between the start and finish year) of each ASI and ENT epoch. The solid boxes indicate 25th and 75th percentiles, and thick red lines in the box is the median value of the persistence time. The whiskers (upper and lower dashed lines) correspond to the 0.7^{th} and 99.3^{th} percentiles of the samples. Asterisk marks (outliers) denote that the persistence time beyond the whisker (0.7^{th} and 99.3^{th} percentiles).

The NPSTMW formation is greatly affected by the local and lagged remote influences of the basin-scale climate variability as mentioned in Section 3.3. To quantify the interannual variability of the atmospheric forcing, the NPSTMW volume in March is compared with the leading PC time series of basin-scale SLP and the EAWM (Figure 47). Following Park et al. (2012), the EAWM is defined as the difference between the area-mean SLP anomalies over the Siberian high

(SH) region (85−105°E, 45−55°N) and southeastern East Sea (135−140°E, 35−40°N). The correlation of the NPSTMW volume and PC-2 (NPO index) for 2000 years is −0.24 with a statistical significance of 95% confidence level (Figure 47b). The other climate indices has weak influence to the variability of the NPSTMW volume ($r_{PC\text{-}1\_NPSTMW}$ = 0.1, and r_{EAWM_NPSTMW} = 0.07) (Figure 47a and 47c).

In order to examine the relationship in two different epochs, the lead-lag correlations are computed over two periods separately: 1140−1180 (ENT epoch) and 1380−1420 (ASI epoch). During the period of 1140−1180 (ENT epoch), the correlation coefficient between the leading PC time series and NPSTMW volume is maximum, when the leading PC time series leads by 4 years (Figure 48a and 48b). As mentioned in Section 3, the 4-year lag indicates that the NPSTMW formation is affected by the first mode baroclinic Rossby wave propagation from the central North Pacific. On the other hands, during the period of 1380−1420 (ASI epoch), the PC-2 and EAWM are correlated with the NPSTMW volume without lag suggesting that the local atmospheric forcing like the EAWM has a strong influence on the NPSTMW variability (Figure 49b and 49c). It is noted that the EAWM and NPO are significantly correlated (r = −0.47) to each other during the ASI epoch (1380−1420), which is consistent with Pak et al. (2014), who showed the significant relationship between the EAWM and NPO during the strong winter monsoon epoch (1973−1987). This is also consistent with the result of the OGCM, which showed the simultaneous and lagged responses of the NPSTMW volume to the NPO in two different epochs.
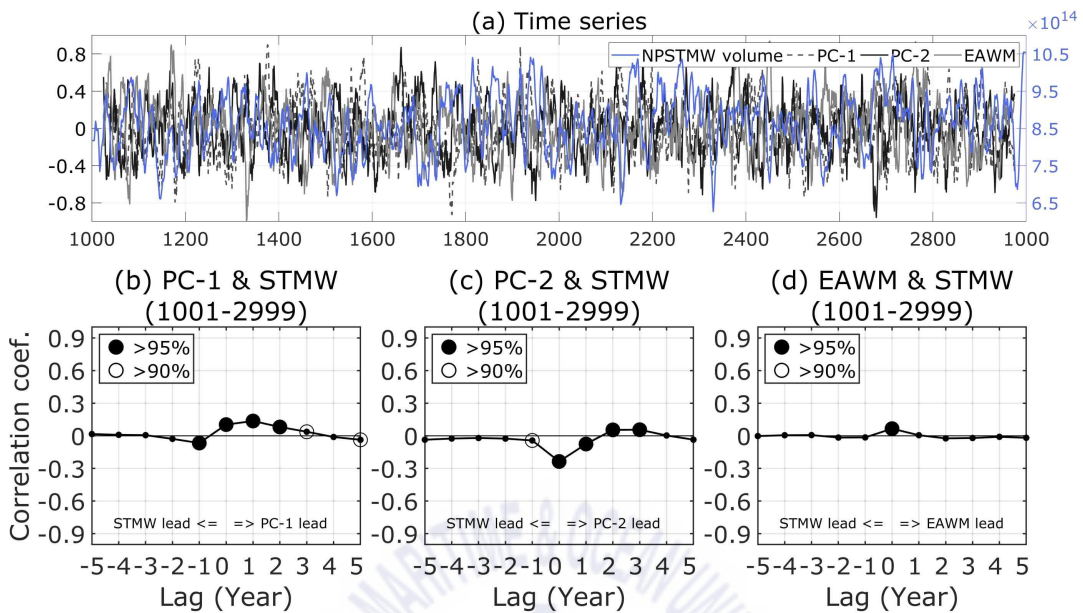
Figure 47. (a) Time series of the NPSTMW volume in March (blue), the EOF PC-1 (dashed black), the PC-2 (solid black), and the EAWM (solid gray). (b) Lead-lag correlation between the NPSTMW volume in March and the EOF PC-1 of SLP during 1001−2999. Positive lag indicates that the EOF PC-1 leads the NPSTMW volume. Closed and open circles indicate significant values at the 95% and 90% confidence level, respectively. As in (b), but for the (c) EOF PC-2 and (d) the EAWM.
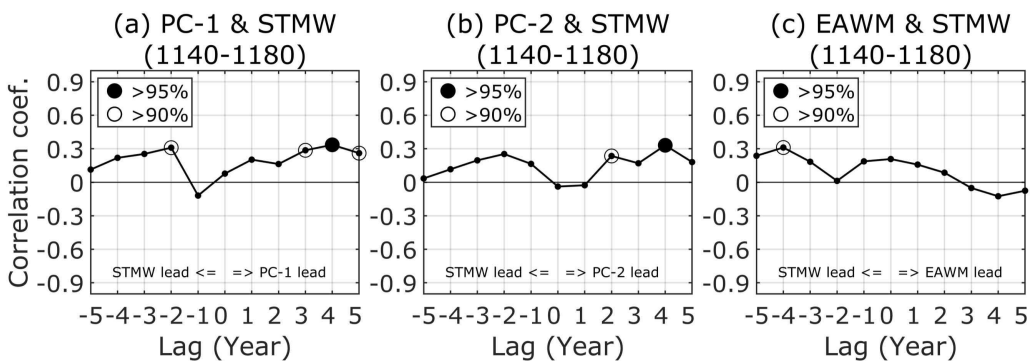
Figure 48. (a) Lead-lag correlation between the NPSTMW volume in March and

the EOF PC-1 of SLP during 1140−1180. Positive lag indicates that the EOF PC-1 leads the NPSTMW volume. Closed and open circles indicate significant values at the 95% and 90% confidence level, respectively. As in (a), but for the (b) EOF PC-2 and (c) the EAWM.
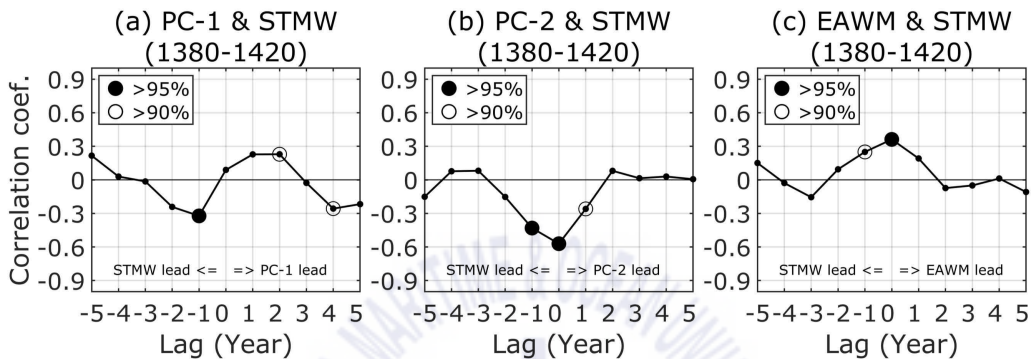
Figure 49. As in Figure 21, but for the time period of 1380−1420.

The composite maps of the winter SLP, surface winds, air temperature and SST in two different epochs can support to understand the background conditions, which causes the regime shift of the NPSTMW formation. Comparing the horizontal distribution of the winter SLP and surface winds between the ASI and ENT epoch (Figure 50a and 50b), there are two distinct features: (1) a weakened AL and (2) a strengthened of southern boundary of the Siberian high during the ASI epoch. During ASI epoch, enhanced northwesterly winds flow over the latitude band from 20°N to 35°N. The surface air temperature abruptly decreases in the subtropical region, especially in the Kuroshio-Oyashio Extension region, along with the strong northwesterly (Figure 50d). Cooling of the surface air temperature in the subtropical region induces the decease of the SST in that region (Figure 50f). This is consistent with Pak et al. (2014) who showed that the winter SST variability in the western North Pacific is under the influence of the mutually correlated EAWM and

NPO patterns before the 1987/1988 regime shift. Therefore, the NPSTMW volume variability is likely dominated by local air-sea interaction during the ASI epoch.
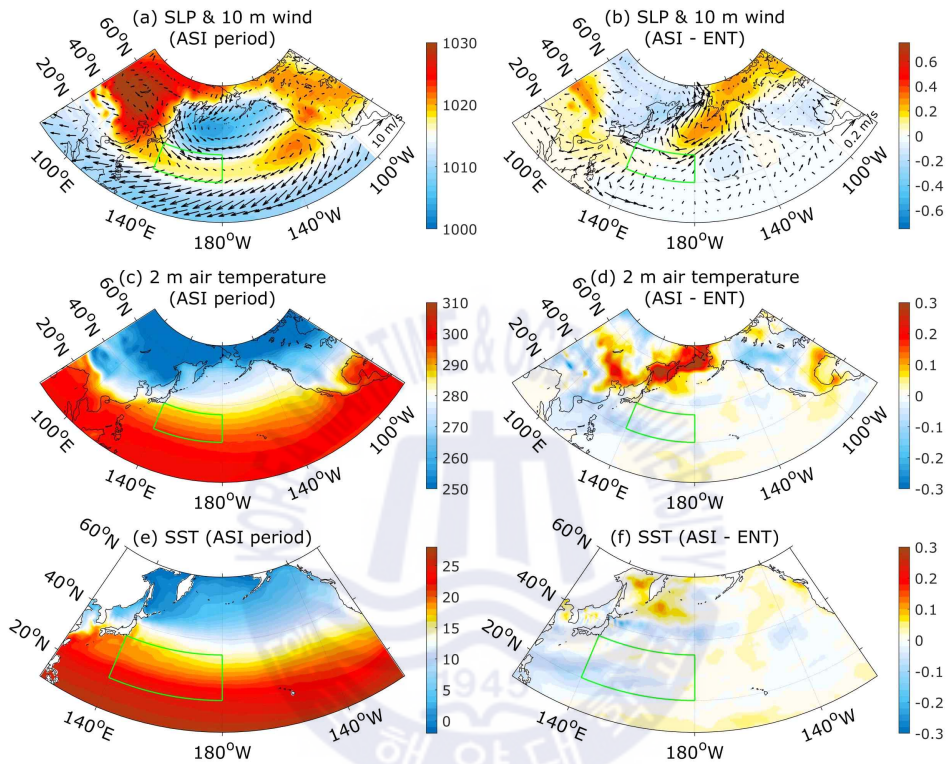
Figure 50. Composite maps of (a) the winter SLP (hPa) and 10 m winds (m s^{-1}), (c) 2 m air temperature (K), and (e) SST (°C) in the ASI period. The differences of (b) the winter SLP and 10 m winds, (d) 2 m air temperature, (f) SST between the ASI and the ENT period.

Chapter 5. Summary and discussion

A regime shift in the formation mechanisms of the NPSTMW as well as its causes is investigated using a OGCM hindcast and an atmosphere-ocean coupled model (KCM). A 50-year (1960−2009) hindcast of the OGCM reproduces well the features of the NPSTMW formation during cooling seasons and its epoch-dependent variability. Based on the moving correlation analysis, it is found that there is change in the main driving mechanism for the interannual variability of the NPSTMW volume in March around late-1980s. During 1962−1982, the local air-sea flux is primarily responsible for the most of the interannual variability of the NPSTMW volume, while it is mostly controlled by ocean dynamics associated with the westward propagating Rossby waves during 1988−2008. The NPSTMW volume has a statistically significant correlation with the NPO over the entire period, though the time lag is different in the two periods. In addition to the changes in the correlation, the changes in the relative amplitudes of the ocean dynamics and air-sea flux terms also contribute to this epoch-dependent formation mechanism of the NPSTMW. The change in the amplitude of variability in these terms is shown to be associated with the differences in the AL variability and WSC during the two periods. During the earlier epoch, with the weak remote signals, a strong local air-sea interaction in the western North Pacific primarily contributes to the formation of the NPSTMW. On the other hands, during the later epoch, the local air-sea interaction is weakened and a strong remote signal driven by large meridional variation of the WSC-zero line propagates westward to the NPSTMW formation area, thus affects the NPSTMW volume change. The change of WSC is related to the meridional shift of the AL center.

A 2,000-year simulation of the atmosphere-ocean coupled model (KCM) reproduces well the features of the NPSTMW formation during cooling seasons and its epoch-dependent variability. In addition, the KCM simulates well the winter SLP

distribution, the surface wind fields, and the AL variability in the North Pacific region. The NPSTMW volume has a statistically significant correlation with the NPO over the entire period. It is found that the transitions of the driving mechanisms for the NPSTMW formation is periodically occurred in multi-decadal timescales and each forcing mechanism persists during about 10−30 years. During the ENT epoch, the north-south shift of the AL center is much wider. During the ASI epoch, strong wind and cold air outbreak from the Siberia much influence on the NPSTMW formation region.

Figure 51 shows a schematic map on the different background conditions for the NPSTMW formation in two regimes. (1) Strong (weak) meridional shift of the AL center during the ENT (ASI) epoch. (2) The meridional shift of the AL center induces the change of zero-WSC line in north-south direction. (3) The WSC anomalies driven by the meridional shift of the AL can induce the change of SSH and isopycnal thickness in the pycnocline via Ekman pumping/suction. (4) Large (small) signals propagate westward via first-mode baroclinic Rossby wave during ENT (ASI) epoch. (5) Oceanic heat loss, which is associated with the EAWM, increases (decreases) during the ASI (ENT) epoch (Pak et al., 2014, 2019; Park et al., 2012). (6) The NPSTMW formation is mainly determined by the ocean dynamics driven by remote forcing (loacl air-sea interaction) during the ENT (ASI) epoch.
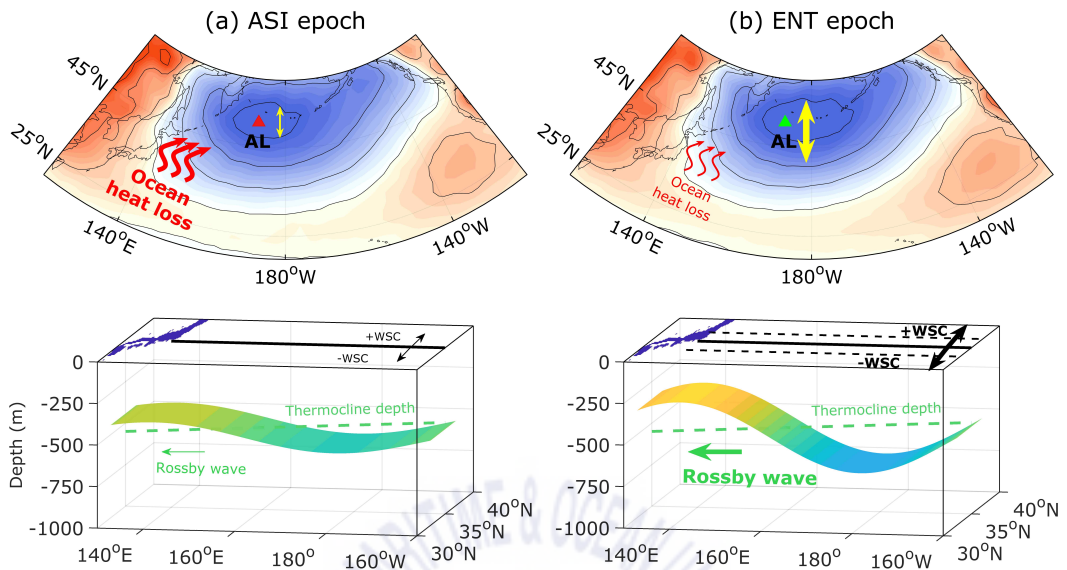
Figure 51. Schematic map showing background conditions for the regime shift of the NPSTMW formation.

The findings in this study are in line with the previous studies showing the regime shift of the upper-ocean thermal states, such as the MLD (Sugimoto & Kako, 2016) and the SST (Pak et al., 2014, 2019; Park et al., 2012), occurred in late-1980s. However, these studies do not focus on the "NPSTMW water mass" itself. Although Sugimoto and Kako (2016) investigated nonstationary driving mechanism for the decadal changes of the winter MLD variability, the MLD alone cannot explain the formation mechanism of the NPSTMW, because the NPSTMW formation is affected by various oceanic processes like the variation of thermocline depth, which can also be driven by the propagation of the remote signal. In this study, it is explicitly investigated the interannual variability of the NPSTMW formation using the volume budget analysis and find a regime shift of the driving mechanism for the NPSTMW formation in late-1980s. The importance of this study is that late-1980s regime shift in the formation mechanism of the NPSTMW is

reported for the first time. In addition, this study provides robust complementary evidences to support the previous observational results by using a long-term eddy-permitting OGCM simulation.

There are several unsolved questions from this study. For example, possible mechanisms for the significant correlation between the basin-scale climate variability and the NPSTMW volume, when the latter leads the former by several years (Figure 20c), are not yet clear. Although, the detailed mechanism is not investigated in this study, there is some evidence of the delayed response of the SST in the central North Pacific to the NPSTMW in the northwestern Pacific. Figure 52 shows the correlation coefficient of the NPSTMW volume in March and the SST in the next year March during two epochs. The response of the SST on the NPSTMW is different in the two regime state. During the ASI epoch, the correlation between two is insignificant in the study area (Figure 52a), this may be related to the strong local air-sea interaction during this periods, which can erase the re-emergenced signal (Pak et al., 2019). On the other hands, during the ENT epoch (1988−2008), the SST is significantly correlated with the NPSTMW volume in the KE region and the central Pacific region as well, suggesting that the NPSTMW affects year to year variation of the SST in the remote area as well as the local area. Since the NPSTMW is subducted below the seasonal thermocline with the memories of the wintertime information during the warm season; thus, it could affect the SST in the remote area from year to year. This remote effect of the NPSTMW can also induce the basin-scale climate variability, such as the NPO shown in Figure 20c, which should be the topic of further study.

Figure 53 shows the relationship between the MLD in March and the SST in the next year March. During the ENT epoch, the correlation is relatively high in the formation area compared with that in the ASI epoch but the remote response of the SST, which we can see in Figure 52, is insignificant in the case of MLD. This result can support why the NPSTMW is important to understand the relationship

between the upper-ocean thermal state in the KE region and the basin-scale climate variability in the North Pacific. Therefore, the variability of the NPSTMW formation may be important for understanding the oceanic impact on the long-term climate variability.
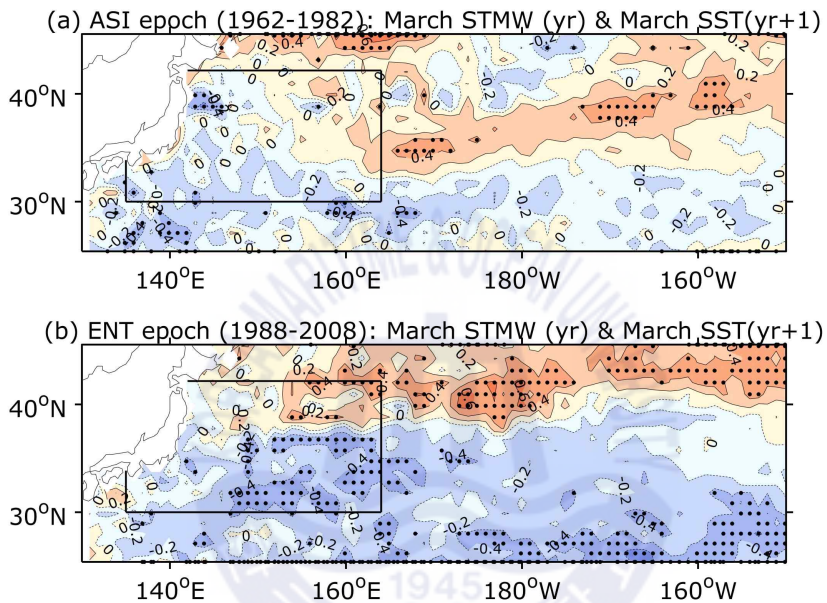
Figure 52. (a) Correlation coefficient between the NPSTMW volume in March and the SST in next year March during the ASI epoch (1962−1982). Black dots indicate regions where the correlation coefficients are statistically significant at the 95% confidence level. (b) Same as in (a), but for the ENT epoch (1988−2008).
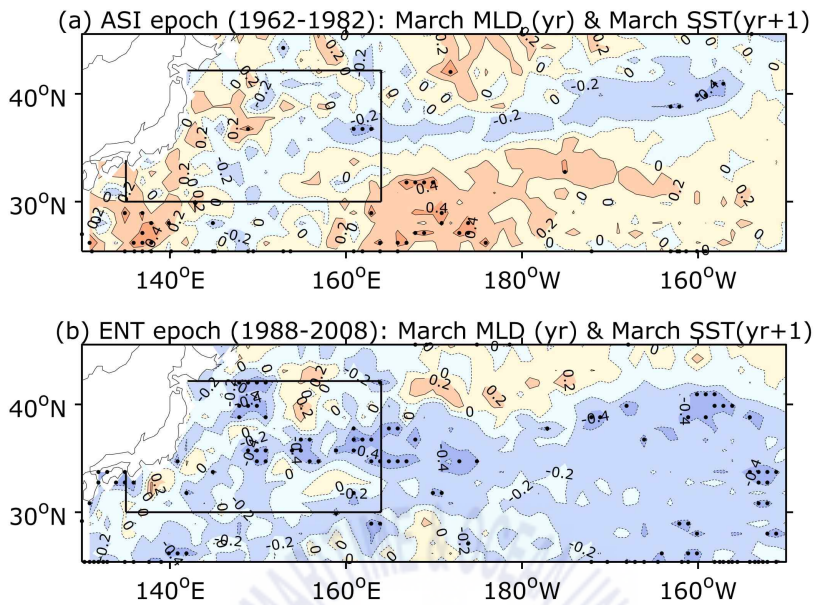
Figure 53. Same as in Figure 52, but for the MLD.

Several previous studies suggested that the local ocean current (KE) instability also affects the variability of the low PV water volume in the KE region (Oka et al., 2019; Qiu & Chen, 2006; Xu et al., 2014). In this study, the relationship between the NPSTMW variability and the variability of the KE position has not been specifically investigated, though the meridional movement of the KE axis is significantly correlated with the NPSTMW volume when the KE leads by 1 year ($r = 0.52$) (Figure 54). More importantly, the two are much better correlated in the later epoch, which implies that the change of the KE position is a part of the increased ocean dynamics contribution in the later epoch. After late-1980s, both time series show an obvious decadal variation, which is similar to that of the meridional variation of the AL center (Figure 24a). It is reasonable because the variability of the KE is highly correlated with the meridional variation of the WSC associated with the AL pressure system (Kwon & Deser, 2007).

Whether the instability of KE, which can change the local ocean stratification, specifically plays a role needs to be further investigated in the future. Further study is also needed to identify the effect of the ocean stratification on the NPSTMW formation, because the ocean stratification is closely related with the local PV field (Qiu & Chen, 2006). Although the strength and path length of the KE also have marginally significant correlations with the NPSTMW volume when each KE dynamics leads the NPSTMW volume by 1 year (Figure 55 and Figure 56), the strength and path length of the KE are underestimated due to unrealistic eddy fields in the eddy-permitting OGCM compared to those of the observational analyses by Qiu et al. (2014, see their Figure 3). To reveal the effect of the ocean stratification associated with the instability of KE on the NPSTMW formation, it is necessary to simulate the high-resolution eddy-resolving OGCM to reproduce a realistic local eddy activity in the KE region. In addition, the high-resolution ocean reanalysis data can also be helpful to detect the features not reproduced by the coarse-resolution ocean model.
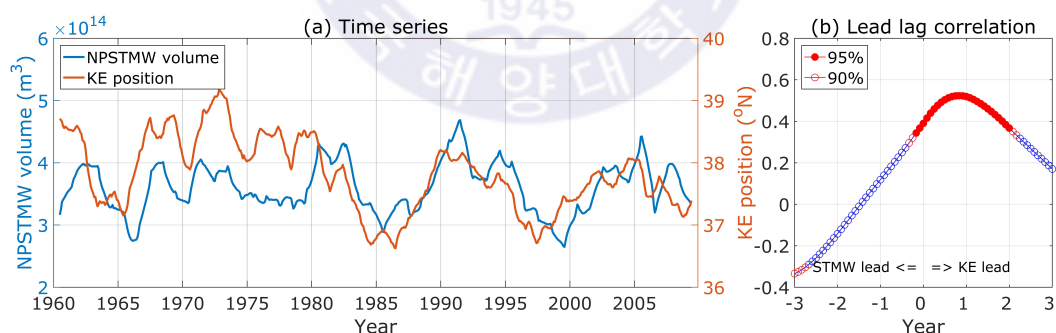
Figure 54. (a) Time series of the 12-month moving averaged NPSTMW volume (blue) and the latitudinal position of the Kuroshio main axis zonally averaged from 141°E to 158°E (red). Kuroshio main axis is defined by the 40-cm contour of the sea surface height. (b) Lead-lag correlation between the latitudinal position of the Kuroshio main axis and the NPSTMW volume. Positive lag indicates that the

latitudinal position of the Kuroshio main axis leads the NPSTMW volume. Closed and open red circles indicate significant values at the 95% and 90% confidence level, respectively.
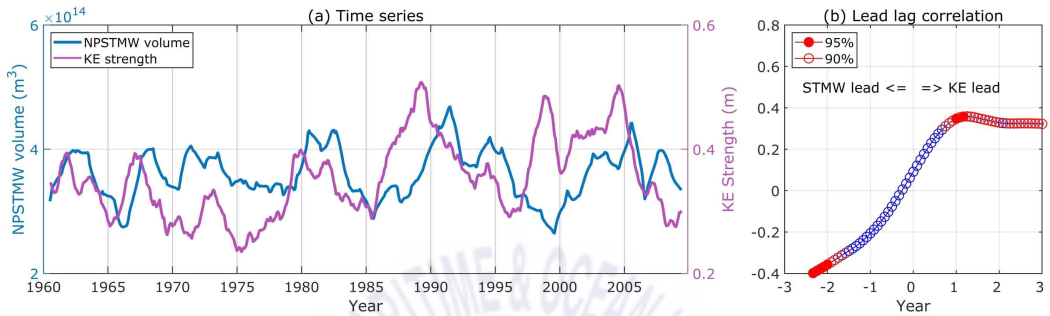
Figure 55. Same as in Figure 54, but for the KE strength, which is defined by the zonal-mean (140–165°E) SSH difference (SSH_{South}–SSH_{North}) between 1° south and 1° north of the KE main axis.
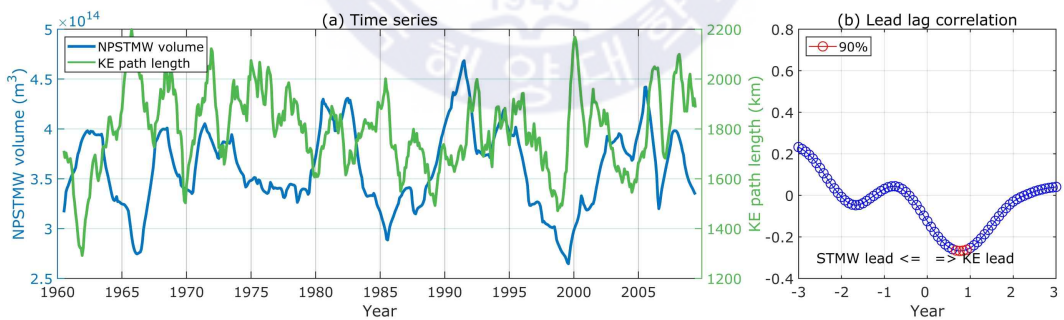
Figure 56. Same as in Figure 54, but for the path length (141–153°E) of the KE main axis.

Acknowledgements

References

Adcroft, A., & Campin, J. M. (2004). Rescaled height coordinates for accurate representation of free-surface flows in ocean circulation models. *Ocean Modelling*, 7(3-4), 269-284. https://doi.org/10.1016/j.ocemod.2003.09.003

Adcroft, A., Hill, C., & Marshall, J. (1997). Representation of topography by shaved cells in a height coordinate ocean model. *Monthly Weather Review*, 125(9), 2293-2315. https://doi.org/10.1175/1520-0493(1997)125<2293:ROTBSC>2.0.CO;2

Alexander, M. A., Deser, C., & Timlin, M. S. (1999). The reemergence of SST anomalies in the North Pacific Ocean. *Journal of Climate*, 12(8), 2419-2433. https://doi.org/10.1175/1520-0442(1999)012<2419:TROSAI>2.0.CO;2

Antonov, J. I., Seidov, D., Boyer, T. P., Locarnini, R. A., Mishonov, A. V., Garcia, H. E., et al. (2010). In S. Levitus (Ed.), *World Ocean Atlas 2009, vol. 2, Salinity*, NOAA Atlas NESDIS (Vol. 69, p. 184). Silver Spring, MD: NOAA.

Arakawa, A., & Lamb, V. R. (1977). Computational design of the basic dynamical processes of the UCLA general circulation model. *Methods in Computational Physics: Advances in Research and Applications*, 17, 173-265. https://doi.org/10.1016/B978-0-12-460817-7.50009-4

Barnston, A. G., & Livezey, R. E. (1987). Classification, seasonality and persistence of low-frequency atmospheric circulation patterns. *Monthly Weather Review*, 115(6), 1083-1126. https://doi.org/10.1175/1520-0493(1987)115<1083:CSAPOL>2.0.CO;2

Bates, N. R. (2012). Multi-decadal uptake of carbon dioxide into subtropical mode water of the North Atlantic Ocean. *Biogeosciences*, 9(7), 2649-2659. https://doi.org/10.5194/bg-9-2649-2012

Bingham, F. M. (1992). Formation and spreading of subtropical mode water in the North Pacific. *Journal of Geophysical Research*, 97(C7), 11,177-11,189.

https://doi.org/10.1029/92JC01001

Ceballos, L. I., Di Lorenzo, E., Hoyos, C. D., Schneider, N., & Taguchi, B. (2009). North Pacific gyre oscillation synchronizes climate fluctuations in the eastern and western boundary systems. *Journal of Climate*, 22(19), 5163–5174. https://doi.org/10.1175/2009JCLI2848.1

Cerovečki, I., & Giglio, D. (2016). North Pacific subtropical mode water volume decrease in 2006–09 estimated from Argo observations: Influence of surface formation and basin-scale oceanic variability. *Journal of Climate*, 29(6), 2177–2199. https://doi.org/10.1175/JCLI-D-15-0179.1

Colella, P., & Woodward, P. R. (1984). The piecewise parabolic method (PPM) for gas-dynamical simulations. *Journal of Computational Physics*, 54(1), 174–201. https://doi.org/10.1016/0021-9991(84)90143-8

Cushman-Roisin, B. (1987). Subduction, in dynamics of the oceanic surface mixed layer, edited by P. Muller and D. Henderson, pp. 181–196, Hawaii Inst. of Geophysical Special Publications.

Davis, X. J., Rothstein, L. M., Dewar, W. K., & Menemenlis, D. (2011). Numerical investigation of seasonal and interannual variaibility of North Pacific subtropical mode water and its implications for Pacific climate variability. *Journal of Climate*, 24(11), 2648–2665. https://doi.org/10.1175/2010JCLI3435.1

Delworth, T. L., Rosati, A., Anderson, W., Adcroft, A. J., Balaji, V., Benson, R., et al. (2012). Simulated climate and climate change in the GFDL CM2.5 high-resolution coupled climate model. *Journal of Climate*, 25(8), 2755–2781. https://doi.org/10.1175/JCLI-D-11-00316.1

Deser, C. & Phillips, A. S. (2009). Atmospheric circulation trends, 1950–2000: The relative roles of sea surface temperature forcing and direct atmospheric radiative forcing. *Journal of Climate*, 22(2), 396–413. https://doi.org/10.1175/2008jcli2453.1

Douglass, E. M., Jayne, S. R., Peacock, S., Bryan, F. O., & Maltrud, M. E. (2012). Subtropical mode water variability in a climatologically forced model in the northwestern Pacific Ocean. *Journal of Physical Oceanography*, 42(1), 126‒140. https://doi.org/10.1175/2011JPO4513.1

Emery, W. J., & Thomson, R. E. (1997). *Data Analysis Methods in Physical Oceanography*. Pergamon, 638 pp.

Fu, L.-L. & Qiu, B. (2002). Low-frequency variability of the North Pacific Ocean: The roles of boundary- and wind-driven baroclinic Rossby waves. *Journal of Geophysical Research*, 107(C12), 3220. https://doi.org/10.1029/2001JC001131

Gillett, N. P., Zwiers, F. W., Weaver, A. J., and Stott P. A. (2003). Detection of human influence on sea-level pressure. *Nature*, 422(6929), 292‒294. https://doi.org/10.1038/nature01487

Good, S. A., Martin, M. J., & Rayner, N. A. (2013). EN4: Quality controlled ocean temperature and salinity profiles and monthly objective analyses with uncertainty estimates. *Journal of Geophysical Research: Oceans*, 118, 6704‒6716. https://doi.org/10.1002/2013JC009067

Griffies, S. M., & Hallberg, R. W. (2000). Biharmonic friction with a Smagorinsky viscosity for use in large-scale eddy-permitting ocean models. *Monthly Weather Review*, 128(8), 2935‒2946. https://doi.org/10.1175/1520-0493(2000)128<2935:BFWASL>2.0.CO;2

Guo, Y., Lin, X., Wei, M., Liu, C., & Men, G. (2018). Decadal variability of North Pacific eastern subtropical mode water. *Journal of Geophysical Research: Oceans*, 123, 6189‒6206. https://doi.org/10.1029/2018JC013890

Hanawa, K. (1987). Interannual variations of the winter-time outcrop area of subtropical mode water in the western North Pacific ocean. *Atmosphere-Ocean*, 25(4), 358‒374. https://doi.org/10.1080/07055900.1987.9649280

Hanawa, K., & Hoshino, I. (1988). Temperature structure and mixed layer in the Kuroshio region over the Izu Ridge. *Journal of Marine Research*, 46(4), 683–700. https://doi.org/10.1357/002224088785113397

Holte, J., Talley, L. D., Gilson, J., & Roemmich, D. (2017). An Argo mixed layer climatology and database. Geophysical Research Letters, 44, 5618–5626. https://doi.org/10.1002/2017GL073426

Ishi, Y. & Hanawa, K. (2005). Large-scale variabilities of wintertime wind stress curl field in the North Pacific and their relation to atmospheric teleconnection patterns. *Geophysical Research Letters*, 32(10), L10607. https://doi.org/2004GL022330

Kobashi, F., Mitsudera, H., & Xie, S.-P. (2006). Three subtropical fronts in the North Pacific: Observational evidence for mode waterinduced subsurface frontogenesis. *Journal of Geophysical Research*, 111, C09033. https://doi.org/10.1029/2006JC003479

Kwon, Y.-O., & Deser, C. (2007). North Pacific decadal variability in the Community Climate System model version 2. *Journal of Climate*, 20(11), 2416–2433. https://doi.org/10.1175/JCLI4103.1

Kwon, Y.-O., Alexander, M. A., Bond, N. A., Frankignoul, C., Nakamura, H., Qiu, B., & Thompson, L. (2010). Role of the Gulf Stream and Kuroshio-Oyashio systems in large-scale atmosphere-ocean interaction: A review. *Journal of Climate*, 23(12), 3249–3281. https://doi.org/10.1175/2010JCLI3343.1

Large, W. G., McWilliams, J. C., & Doney, S. C. (1994). Oceanic vertical mixing: A review and a model with a nonlocal boundary layer parameterization. *Reviews of Geophysics*, 32(4), 363–403. https://doi.org/10.1029/94RG01872

Large, W. G., & Yeager, S. G. (2004). Diurnal to decadal global forcing for ocean and sea-ice models: The data sets and flux climatologies (NCAR Tech. Rep.

TN-460+STR, 105 pp.). National Center for Atmospheric Research, Colo.

Large, W. G., & Yeager, S. G. (2009). The global climatology of an interannually varying air-sea flux data set. *Climate Dynamics*, 33(2–3), 341–364. https://doi.org/10.1007/s00382-008-0441-3

Lee, H.-C., Rosati, A., & Spelman, M. J. (2006). Barotropic tidal mixing effects in a coupled climate model: Oceanic conditions in the Northern Atlantic. *Ocean Modelling*, 11(3–4), 464–477. https://doi.org/10.1016/j.ocemod.2005.03.003

Levitus, S., et al. (1998). *World Ocean Data Base 1998*. NOAA Atlas NESDIS 18, 346 pp.

Linkin, M. E., & Nigam, S. (2008). The North Pacific Oscillation-west Pacific teleconnection pattern: Mature-phase structure and winter impacts. *Journal of Climate*, 21(9), 1979–1997. https://doi.org/10.1175/2007JCLI2048.1

Locarnini, R. A., Mishonov, A. V., Antonov, J. I., Boyer, T. P., Garcia, H. E., Baranova, O. K., et al. (2010). In S. Levitus (Ed.), *World Ocean Atlas 2009, vol. 1, Temperature*, NOAA Atlas NESDIS (Vol. 69, p. 184). Silver Spring, MD: NOAA.

Lu, J., Greatbatch, R. J., and Peterson, K. A. (2004). Trend in Northern Hemishpere winter atmospheric circulation during the last half of the twentieth century. *Journal of Climate*, 17(19), 3745–3760. https://doi.rog/10.1175/1520-0442(2004)017<3745:tinhwa>2.0.co;2

Madec, G. (2008). NEMO reference manual, ocean dynamics component: NEMO-OPA. Preliminary version, *Note Pole Model, 27*, Inst. Pierre-Simon Laplace, Paris.

Masumoto, Y., Sasaki, H., Kagimoto, T., Komori, N., Ishida, A., Sasai, Y., et al. (2004). A fifty-year eddy-resolving simulation of the world ocean: Preliminary outcomes of OFES (OGCM for the Earth Simulator). *Journal of the Earth*

Simulator, 1, 35–56.

Masuzawa, J. (1969). Subtropical mode water. *Deep Sea Research and Oceanographic Abstracts*, 16(5), 463–472. https://doi.org/10.1016/0011-7471(69)90034-5

Murray, R. J. (1996). Explicit generation of orthogonal grids for ocean models. *Journal of Computational Physics*, 126(2), 251–273. https://doi.org/10.1006/jcph.1996.0136

Na, H., Kim, K.-Y., Minobe, S., & Sasaki, Y. N. (2018). Interannual to decadal variability of the upper-ocean heat content in the western North Pacific and its relationship to oceanic and atmospheric variability. *Journal of Climate*, 31(13), 5107–5125. https://doi.org/10.1175/JCLI-D-17-0506.1

Nishikawa, S., Tsujino, H., Sakamoto, K, & Nakano, H. (2013). Diagnosis of water mass transformation and formation rates in a high-resolution GCM of the North Pacific. *Journal of Geophysical Research: Oceans*, 118(3), 1051–1069. https://doi.org/10.1029/2012JC008116

Nurser, A. J. G., Marsh, R., & Williams, R. G. (1999). Diagnosing water mass formation from air-sea fluxes and surface mixing. *Journal of Physical Oceanography*, 29(7), 1468–1487. https://doi.org/10.1175/1520-0485(1999)029<1468:DWMFFA>2.0.CO;2

Oka, E., & Qiu, B. (2012). Progress of North Pacific mode water research in the past decade. *Journal of Oceanography*, 68(1), 5–20. https://doi.org/10.1007/s10872-011-0032-5

Oka, E., Yamada, K., Sasano, D., Enyo, K., Nakano, T., & Ishii, M. (2019). Remotely forced decadal physical and biogeochemical variability of North Pacific subtropical mode water over the last 40 years. *Geophysical Research Letters*, 46, 1555–1561. https://doi.org/10.1029/2018GL081330

Pacanowski, R. C., & Gnanadesikan, A. (1998). Transient response in a Z-level ocean model that resolves topography with partial cells. *Monthly Weather Review*, 126(12), 3248–3270. https://doi.org/10.1175/1520-0493(1998)126<3248:TRIAZL>2.0.CO;2

Pak, G., Park, Y.-H., Vivier, F., Kwon, Y.-O., & Chang, K.-I. (2014). Regime-dependent nonstationary relationship between the East Asian winter monsoon and North Pacific Oscillation. *Journal of Climate*, 27(21), 8185–8204. https://doi.org/10.1175/JCLI-D-13-00500.1

Pak, G., Yeh, S.-W., Nam, S., Park, Y.-H., & Kim, Y. H. (2019). Major driver leading to winter SST variability in the Kuroshio recirculation gyre region and its decadal changes: Refreshing versus spring-initiated reemergence processes. *Geophysical Research Letters*, 46, 272–280. https://doi.org/10.1029/2018GL081232

Park, W., Keenlyside, N., Latif, M., Ströh, A., Redler, R., Roeckner, E., and Madec, G. (2009). Tropical Pacific climate and its response to global warming in the Kiel Climate Model. *Journal of Climate*, 22(1), 71–92. https://doi.org/10.1175/2008jcli2261.1

Park, Y.-H., Yoon, J.-H., Youn, Y.-H., & Vivier, F. (2012). Recent warming in the western North Pacific in relation to rapid changes in the atmospheric circulation of the Siberian high and Aleutian low systems. *Journal of Climate*, 25(10), 3476–3493. https://doi.org/10.1175/2011JCLI4142.1

Qiu, B. (2003). Kuroshio Extension variability and forcing of the Pacific Decadal Oscillations: Responses and potential feedback. *Journal of Physical Oceanography*, 33(12), 2465–2482. https://doi.org/10.1175/2459.1

Qiu, B., & Chen, S. (2006). Decadal variability in the formation of the North Pacific subtropical mode water: Oceanic versus atmospheric control. *Journal of Physical Oceanography*, 36(7), 1365–1380. https://doi.org/10.1175/JPO2918.1

Qiu, B., Chen, S. & Hacker, P. (2007). Effect of mesoscale eddies on subtropical mode water variability from the Kuroshio Extension System Study (KESS). *Journal of Physical Oceanography*, 37(4), 982‑1000. https://doi.org/10.1175/JPO3097.1

Qiu, B., & Chen, S. (2010). Eddy‑mean flow interaction in the decadal modulating Kuroshio Extension system. *Deep Sea Research, Part II*, 57(13‑14), 1098‑1110. https://doi.org/10.1016/j.dsr2.2008.11.036

Qiu, B., Chen, S., Schneider, N., & Taguchi, B. (2014). A coupled decadal prediction of the dynamic state of the Kuroshio Extension system. *Journal of Climate*, 27(4), 1751‑1764. https://doi.org/10.1175/JCLI‑D‑13‑00318.1

Rainville, L., Jayne, S. R., McClean, J. L., & Maltrud, M. E. (2007). Formation of subtropical mode water in a high‑resolution ocean simulation of the Kuroshio Extension region. *Ocean Modelling*, 17(4), 338‑356. https://doi.org/10.1016/j.ocemod.2007.03.002

Rainville, L., Jayne, S. R., & Cronin, M. F. (2014). Variations of the North Pacific subtropical mode water from direct observations. *Journal of Climate*, 27(8), 2842‑2860. https://doi.org/10.1175/JCLI‑D‑13‑00227.1

Roeckner, E., et al. (2003). The atmospheric general circulation model ECHAM5. Part I: Model description, *Rep. 349*, 127 pp., Max Planck Inst. for Meteorol., Hamburg, Germany.

Simmons, H. L., Jayne, S. R., Laurent, L. C. S., & Weaver, A. J. (2004). Tidally driven mixing in a numerical model of the ocean general circulation. *Ocean Modelling*, 6(3‑4), 245‑263. https://doi.org/10.1016/S1463‑5003(03)00011‑8

Speer, K., & Tziperman, E. (1992). Rates of water mass formation in the North Atlantic ocean. *Journal of Physical Oceanography*, 22(1), 93‑104. https://doi.org/10.1175/1520-0485(1992)022<0093:ROWMFI>2.0.CO;2

Steele, M., Morley, R., & Ermold, W. (2001). PHC: A global ocean hydrography with a high-quality Arctic Ocean. *Journal of Climate*, 14(9), 2079–2087. https://doi.org/10.1175/1520-0442(2001)014<2079:PAGOHW>2.0.CO;2

Suga, T., & Hanawa, K. (1990). The mixed-layer climatology in the northwestern part of the North Pacific subtropical gyre and the formation area of subtropical mode water. *Journal of Marine Research*, 48(3), 543–566. https://doi.org/10.1357/002224090784984669

Sugimoto, S., & Hanawa, K. (2005). Remote reemergence areas of winter sea surface temperature anomalies in the North Pacific. *Geophysical Research Letters*, 32, L01606. https://doi.org/10.1029/2004gl021410

Sugimoto, S. & Hanawa, K. (2007). Further evidence for non-reemergence of winter SST anomalies in the North Pacific eastern subtropical mode water area. *Journal of Oceanography*, 63, 625–635. https://doi.org/10.1007/s10872-007-0055-0

Sugimoto, S. & Hanawa, K. (2009). Decadal and interdecadal variations of the Aleutian Low activity and their relation to upper oceanic variations over the North Pacific. *Journal of the Meteorological Society of Japan*, 87(4), 601–614. https://doi.org/10.2151/jmsj.87.601

Sugimoto, S., & Hanawa, K. (2010). Impact of Aleutian Low activity on the STMW formation in the Kuroshio recirculation gyre region. *Geophysical Research Letters*, 37, L03606. https://doi.org/10.1029/2009GL041795

Sugimoto, S., & Kako, S. (2016). Decadal variation in winter mixed layer depth south of the Kuroshio Extension and its influence on winter mixed layer temperature. *Journal of Climate*, 29(3), 1237–1252. https://doi.org/10.1175/JCLI-D-15-0206.1

Sverdrup, H. U. (1947). Wind-driven currents in a baroclinic ocean; with application to the Equatorial currents of the Eastern Pacific. *Proceedings of the*

National Academy of Sciences of the United States of America, 33(11), 318–326. https://doi.org/10.1073/pnas.33.11.318

Torrence, C. & Compo, G. P. (1998). A practical guide to wavelet analysis. *Bulletin of the American Meteorological Society*, 79(1), 61–78. https://doi.org/10.1175/1520-0477(1998)079<0061:APGTWA>2.0.CO;2

Toyoda, T., Awaji, T., Ishikawa, Y., & Nakamura, T. (2004). Preconditioning of winter mixed layer in the formation of north Pacific eastern subtropical mode water. *Geophysical Research Letters*, 31, L17206. https://doi.org/10.1029/2004GL020677

Trenberth, K. E., & Hurrell, J. W. (1994). Decadal atmosphere–ocean variations in the Pacific. *Climate Dynamics*, 9(6), 303–319. https://doi.org/10.1007/BF00204745

Tsubouchi, T., Suga, T., & Hanawa, K. (2016). Comparison study of subtropical mode waters in the world ocean. *Frontiers in Marine Science*, 3, 270. https://doi.org/10.3389/fmars.2016.00270

Tsujino, H., & Yasuda, T. (2004). Formation and circulation of mode water of the north Pacific in a high–resolution GCM. *Journal of Physical Oceanography*, 34(2), 399–415. https://doi.org/10.1175/1520-0485(2004)034<0399:FACOMW>2.0.CO;2

Valcke, S. (2006). OASIS3 user guide, *PRISM Tech. Rep. 3*, 64 pp., Partnership for Res. Infrastructures in Earth Syst. Model., Toulouse, France.

Von Storch, H., & Zwiers, F. W. (1999). *Statistical analysis in climate research* (p. 494). Cambridge: Cambridge University Press.

Walin, G. (1982). On the relation between sea surface heat flow and thermal circulation in the ocean. *Tellus*, 34(2), 187–195. https://doi.org/10.3402/tellusa.v34i2.10801

Wallace, J. M., & Gutzler, D. S. (1981). Teleconnections in the geopotential height field during the northern hemisphere winter. *Monthly Weather Review*, 109(4), 784

−812. https://doi.org/10.1175/1520‑0493(1981)109<0784:TITGHF>2.0.CO;2

Xu, L., Xie, S.-P., McClean, J. L., Liu, Q., & Sasaki, H. (2014). Mesoscale eddy effects on the subduction of North Pacific mode waters. *Journal of Geophysical Research: Oceans*, 119, 4867−4886. https://doi.org/10.1002/2014JC009861

Yeh, S.-W., Yi, D.-W., Sung, M.-K., & Kim, Y. H. (2018). An eastward shift of the North Pacific Oscillation after the mid‑1990s and its relationship with ENSO. *Geophysical Research Letters*, 45, 6654−6660. https://doi.org/10.1029/2018GL078671